

# Migrating diurnal tide anomalies during QBO disruptions in 2016 and 2020: morphology and mechanism

Shuai Liu<sup>1,2</sup>, Guoying Jiang<sup>1,3,4</sup>, Bingxian Luo<sup>1,2</sup>, Xiao Liu<sup>5</sup>, Jiyao Xu<sup>1,3</sup>, Yajun Zhu<sup>1,3,4</sup>, Wen Yi<sup>6,7</sup>

<sup>1</sup>State Key Laboratory of Solar Activity and Space Weather, National Space Science Center, Chinese Academy of Sciences, Beijing, 100190, China

<sup>2</sup>College of Earth and Planetary Sciences, University of Chinese Academy of Sciences, Beijing, 101408, China

<sup>3</sup>School of Astronomy and Space Science, University of Chinese Academy of Sciences, Beijing, 101408, China

<sup>4</sup>Hainan National Field Science Observation and Research Observatory for Space Weather, Danzhou, Hainan Province, China.

<sup>5</sup>School of Mathematics and Statistics, Henan Normal University, Xinxiang, 453007, China

<sup>6</sup>CAS Key Laboratory of Geospace Environment, Department of Geophysics and Planetary Sciences, University of Science and Technology of China, Hefei, China

<sup>7</sup>CAS Center for Excellence in Comparative Planetology, Anhui Mengcheng Geophysics National Observation and Research Station, University of Science and Technology of China, Hefei, China

Correspondence to: Guoying Jiang ([gyjiang@swl.ac.cn](mailto:gyjiang@swl.ac.cn)) and Bingxian Luo ([luobx@nssc.ac.cn](mailto:luobx@nssc.ac.cn))

**Abstract.** The stratosphere Quasi-Biennial Oscillation (QBO) modulates the migrating diurnal tide (DW1) in the mesosphere and lower thermosphere (MLT). DW1 amplitudes are larger during QBO westerly (QBOW) than during easterly (QBOE) phases. Since QBO's discovery in 1953, two rare QBO disruption events occurred in 2016 and 2020. During these events, anomalous westerly winds propagate upward, disrupting normal downward propagation of easterly phase and producing a persistent westerly wind layer. In this study, global responses of DW1 amplitudes and phases in MLT to these QBO disruptions, as well as ~~its~~ their underlying mechanisms are investigated, using SABER/TIMED observations, MERRA-2 reanalysis and SD-WACCM-X simulations. Similarity of the DW1 responses to these two events is that DW1 phases and wavelengths exhibit close results to QBOW, whereas ~~the~~ amplitudes lie between QBOW and QBOE. ~~show significant responses. Relative to regular QBOE, DW1 amplitudes in equatorial MLT (maximum difference) increase vary by -20.5-% and -10.2% relative to QBOE and QBOW at equator and -14.4 % at 30°N/S during the in 2016 event, but by only -6.0-% and -21.1%-and -7.7 % during the in 2020 event. In 2016 event, water-water-vapor radiative and latent heating, jointly modulated by the event and ENSO, increased significantly by -8 % and -22 %-relative to QBOE. The Less dissipation and less tidal energy removal in stratosphere along with zonal wind latitudinal shear and gravity-wave (GW) drag in mesosphere tend to enhance DW1 amplitudes. In contrast, in 2020 event, only water-water-vapor radiative heating exhibits a -5-% increase. The dissipation and tidal energy removal-zonal wind latitudinal shear has adverse-less effect on DW1, while GW drag exerts a comparatively weaker influence. The modest enhancement of water vapor heating together with the weaker GW drag likely accounts for the weaker enhancement of DW1 during this event.~~

## 33 1 Introduction

34 Atmospheric solar tides are planetary-scale harmonic waves with periods of a solar day. In the mesosphere and lower  
35 thermosphere (MLT), solar tides exert significant influences on atmospheric parameters such as wind, temperature, and density  
36 (Chapman & Lindzen, 1980; Xu et al., 2009; Jiang et al., 2010; Smith, 2012). Among these tides, the migrating diurnal tide  
37 (DW1) is one of the most prominent components. DW1 in MLT is modulated by external forcings, including the stratosphere  
38 Quasi-Biennial Oscillation (QBO, Hagan et al., 1999; Wu et al., 2008; Xu et al., 2009; Oberheide et al., 2009; Mukhtarov et  
39 al., 2009; Davis et al., 2013; Gan et al. 2014), El Niño–Southern Oscillation (ENSO, Lieberman et al., 2007; Cen et al., 2022)  
40 and 11-year solar cycle response (Singh and Gurubaran, 2017; Sun et al., 2022; Liu et al., 2024a; Liu et al., 2024b). In this  
41 work, the impact of QBO is focused [on](#).

42 The QBO dominates the variability of the equatorial stratosphere (~16–50 km), shown as alternating downward propagating  
43 easterly wind (so-called QBO easterly phases) and westerly wind (so-called QBO westerly phases), with an averaging period  
44 of approximately 28 months (Baldwin et al., 2001). QBO is driven by vertically propagating Kelvin [waves](#), mixed Rossby  
45 gravity waves and small-scale gravity waves (Lindzen and Holton, 1968; Holton and Lindzen, 1972; Baldwin et al., 2001; Ern  
46 et al., 2014). It could influence the transport and distribution of trace gases like water vapor and ozone in the troposphere and  
47 stratosphere (Schoeberl et al., 2008).

48 During the winter of 2015/16 and 2019/20, two rare stratospheric QBO disruption events occurred, which were found only  
49 twice since the record began in 1953. The events are manifested by anomalous westerly winds propagating upward, disrupting  
50 normal downward propagation of the easterly phase and producing a persistent westerly wind layer (Newman et al., 2016;  
51 Anstey et al., 2021). The 2016 QBO disruption has been confirmed to have a close causal relationship with the 2015/16 extreme  
52 El Niño event (Newman et al., 2016; Osprey et al., 2016; Barton and ~~Meeormaek~~[McCormack](#), 2017; Coy et al., 2017). The  
53 2015/16 El Niño substantially weakened the subtropical easterly jet, allowing enhanced Rossby wave propagation from the  
54 extratropics into the deep tropics near 40 hPa (Barton and ~~Meeormaek~~[McCormack](#), 2017). These amplified Rossby waves  
55 subsequently broke and deposited momentum near the QBO westerly core, rather than at the climatological zero-wind line,  
56 causing a pronounced deceleration. The deceleration gave rise to a persistence of westerlies at 40–15 hPa, preventing the  
57 expected transition to easterlies and ultimately leading to the QBO disruption (Newman et al., 2016; Osprey et al., 2016; Coy  
58 et al., 2017; Barton and ~~Meeormaek~~[McCormack](#), 2017; Kang et al., 2022; Wang et al., 2023). The QBO disruption was  
59 accompanied by a marked strengthening of the Brewer–Dobson residual circulation, thereby intensifying tropical upwelling.  
60 This upwelling contributed to an upward displacement of westerlies in the tropical lower stratosphere (Coy et al., 2017),  
61 modifying the transport and distribution of trace gases such as water vapor. The persistent westerlies also created conducive  
62 background conditions for the vertical propagation of DW1. Nevertheless, not all strong El Niño events trigger QBO  
63 disruptions. In the 2015/16 case, the QBO westerly wind core was weaker and Rossby wave activity [was](#) stronger than in other  
64 extreme events, such as the 1998 El Niño (Barton and ~~Meeormaek~~[McCormack](#), 2017). In [the](#) 2020 event, the upward-  
65 propagating westerly wind ~~was~~[is](#) so weak that the monthly mean zonal wind ~~appeared~~[is shown](#) as upward-propagating easterly

66 wind (e.g., Anstey et al., 2021; Wang et al., 2023). This event ~~is~~was driven by strong extratropical Rossby waves associated  
 67 with the 2019 minor SSW in ~~the southern~~south hemisphere (Kang and Chun, 2021; Wang et al., 2023). In these two events,  
 68 the trace gases ~~such as~~like ozone and water vapor are modulated. During the 2016 QBO disruption event, positive water vapor  
 69 anomalies were observed between the tropopause and lower stratosphere, while positive ozone anomalies appeared in the  
 70 upper stratosphere (Tweedy et al., 2017; Diallo et al., 2018). A similar pattern was reported for the 2020 disruption event, with  
 71 water vapor in the lower stratosphere and ozone in the upper stratosphere also exhibiting positive anomalies (Diallo et al.,  
 72 2022).  
 73 QBO modulation of diurnal tides has been reported by both ground-based and space-borne observations (Araújo et al., 2017;  
 74 Davis et al., 2013; Pramitha et al., 2021b; Wu et al., 2008; Dhadly et al., 2018). Mayr and Mengel (2005) reported that the  
 75 QBO can affect these amplitudes by up to 30-% using the Numerical Spectral Model (NSM). Thermosphere, Ionosphere,  
 76 Mesosphere Energetics and Dynamics/Sounding of the Atmosphere using Broadband Emission Radiometry (TIMED/SABER)  
 77 observations revealed that the quasi-biennial variability of DW1 could exceed 50-% at certain altitudes (Garcia, 2023). The  
 78 modulation was characterized by larger-than-average diurnal tide amplitudes during the westerly phase of the QBO and  
 79 smaller-than-average amplitudes during the easterly phase (Vincent et al., 1998; Wu et al., 2008; Xu et al., 2009; Davis et al.,  
 80 2013; Araújo et al., 2017; Pramitha et al., 2021b; Garcia, 2023). Several mechanisms have been proposed ~~could be considered~~  
 81 for modulating the migrating diurnal tide (DW1). A primary factor emphasized in many studies is the variation in the  
 82 background zonal wind and its latitudinal shear (Forbes and Vincent, 1989; Hagan et al., 1999; McLandress, 2002b; Riggins  
 83 and Lieberman, 2013; Liu et al., 2015; Ortland, 2017; Dhadly et al., 2018; Pramitha et al., 2021a, b). Forbes and Vincent (1989)  
 84 demonstrated that the DW1 (1,1) mode experiences stronger dissipation in easterly phases than in westerly phases, while  
 85 McLandress (2002b) highlighted the tide's strong sensitivity to latitudinal shears in the zonal mean easterlies of the summer  
 86 mesosphere. Apart from the influence of the background wind, additional contributions have been suggested, including  
 87 variations in diurnal heating (McLandress, 2002b; Riggins and Lieberman, 2013; Ortland, 2017) and tide-gravity wave (GW)  
 88 interactions (Mayr et al., 1998; McLandress, 2002a; Lu et al., 2012; Wang et al., 2024), both of which may play a role in  
 89 modulating the QBO-related variability of DW1.  
 90 Recent studies have shown that the diurnal tides were ~~also~~ modulated during the QBO disruption events (Pramitha et al., 2021a;  
 91 Garcia, 2023; Wang et al., 2024). Pramitha et al. (2021a) first reported the enhancement of the diurnal tides during the  
 92 2015/2016 QBO disruption event using a meteor radar over Tirupati (13.63°N, 79.4°E) and linked this enhancement to changes  
 93 in ozone concentration. Garcia (2023) showed the equatorial response of temperature DW1 to these two disruption events  
 94 when analysing the QBO modulation to DW1. Wang et al. (2024) reported the weakened mesospheric diurnal tides at mid-  
 95 latitude during QBO disruption events, which ~~is~~were observed by a meteor radar chain. They further ~~provided~~gave the  
 96 modulation evidence of gravity wave forcing and solar radiative absorption by subtropical stratospheric ozone, as revealed by  
 97 SD-WACCM-X simulations.  
 98 These findings raise three questions: (1) In addition to the equatorial peak, temperature DW1 exhibits secondary amplitude  
 99 maxima at 30°N and 30°S (Xu et al., 2009; Garcia, 2023). Whether the DW1 amplitudes on a global scale show a similar

100 response to the QBO disruption events. (2) Whether the phases and wavelengths of DW1 could be affected by the events. (3) Mechanisms for modulating DW1 include heating sources such as water vapor radiative heating and latent heating, zonal  
101 wind latitudinal shear, and tide-gravity wave interactions (e.g., Forbes and Vincent, 1989; Hagan, 1996; Hagan et al., 1999;  
102 McLandress, 2002a; Kogure and Liu, 2021). Whether these mechanisms play significant roles in modulating DW1 during  
103 QBO disruption events.  
104  
105 The present study will focus on the global response feature of DW1 and its underlying mechanisms to QBO disruption events.  
106 The response of DW1 amplitudes, phases and wavelengths during the event will be investigated. Moreover, the contribution  
107 of possible mechanisms, including heating sources, the zonal wind latitudinal shear and tidal-gravity wave [interaction](#) during  
108 the event, will be explored. The article is organized as follows: Section 2 introduces TIMED/SABER, SD-WACCM-X, [and](#)  
109 MERRA-2 data and the methodologies to extract the migrating tides. Section 3 presents the response feature of the DW1 to  
110 the QBO disruption events revealed by SABER/TIMED observations and SD-WACCM-X simulation results. The possible  
111 mechanism of DW1 response to the disruption events is discussed in Section 4. Section 5 presents the summary.

## 112 **2 Data and methodology**

113 This study employs the dataset of SABER/TIMED observations, SD-WACCM-X simulations and MERRA-2 reanalysis to  
114 reveal the feature of DW1 and its excitation sources during QBO disruption events. DW1 amplitude, phase, and wavelength  
115 are derived from both SABER/TIMED data and SD-WACCM-X outputs. MERRA-2 reanalysis is used to analyse the  
116 contributions of water vapor radiative heating and latent heating to DW1 variability during the QBO disruption events, while  
117 SABER/TIMED observations characterize ozone radiative heating. SD-WACCM-X simulations validate the excitation source  
118 revealed by the observational datasets.

### 119 **2.1 SABER/TIMED observations**

120 The TIMED satellite is in a near sun-synchronous orbit with a  $73^\circ$  inclination at about 625 km. The number of orbits observed  
121 per day is about 15. SABER, an instrument in the TIMED satellite, is a 10-channel broadband (1.27–17  $\mu\text{m}$ ) limb-scanning  
122 infrared radiometer. SABER observations of infrared radiance are used to retrieve kinetic temperature, trace gases, etc. In this  
123 work, kinetic temperature and ozone observations in level 2 A (L2A) dataset and ozone heating rate in level 2B (L2B) dataset  
124 are selected to analyse the DW1 response to QBO disruption events. Kinetic temperature is derived using a full nonlocal  
125 thermodynamic equilibrium (non-LTE) inversion algorithm (Mertens et al., 2001; 2004) with the combination of the measured  
126 15  $\mu\text{m}$   $\text{CO}_2$  vertical emission profile and  $\text{CO}_2$  concentrations provided by the Whole Atmosphere Community Climate Model  
127 (WACCM 3.5.48), [as](#) described ~~in~~ [by](#) Garcia et al. (2007).  
128 It takes SABER 60 days to sample 24 hours in local time. The data latitudinal coverage every 60 days extends from  $53^\circ\text{N}$  to  
129  $83^\circ\text{S}$  or  $53^\circ\text{S}$ – $83^\circ\text{N}$ . Temperature observations taken from version 2.07 data from 2002 to 2019 and version 2.08 data from

2020 to 2023 are used. The details of the version switches could refer to Mlynczak et al. (2022, 2003). The retrieved temperature observations used in this work cover altitudes from approximately 15 km to 105 km.

## 2.2 SD-WACCM-X

The Whole Atmosphere Community Climate Model with thermosphere–ionosphere eXtension (WACCM-X) is a comprehensive numerical model that could simulate the Earth's atmosphere from the surface up to the upper thermosphere (~500–700 km), including the ionosphere (Liu et al., 2010; 2018). WACCM-X is a single, unified whole-atmosphere model that extends the NCAR Whole Atmosphere Community Climate Model (WACCM4; Marsh et al., 2013). WACCM4 itself [was](#) built upon the Community Atmosphere Model 4 (CAM4; Neale et al., 2013). While the thermosphere–ionosphere physics (e.g., global electrodynamics,  $O^+$  transport, electron/ion energetics) incorporated in WACCM-X were largely adapted from the NCAR Thermosphere–Ionosphere–Electrodynamics General Circulation Model (TIE-GCM; Qian et al., 2014; Pedatella, 2022), they have been re-engineered within the WACCM-X dynamical core and coupled to the lower- and middle-atmosphere processes through a dedicated ionosphere-interface module. SD in the SD-WACCM-X means specified dynamics, which is an approach described in Smith et al. (2017). The reanalysis fields from Modern-Era Retrospective analysis for Research and Applications, Version 2 (MERRA-2, Gelaro et al., 2017) data from the surface up to ~50 km are nudged in WACCM-X. Model parameters are output in 3-hour resolution. The latitude-longitude resolution is  $1.9^\circ \times 2.5^\circ$ . The model has 145 pressure levels with a varying vertical resolution of ~1.1–1.75 km in the troposphere and stratosphere and ~3.5 km in the mesosphere. In this work, the temperature, zonal wind, temperature tendency due to moist process and long wave heating rate ranging from 2002 to 2022 are selected.

## 2.3 MERRA-2

MERRA-2 is a reanalysis product from the NASA Global Modeling and Assimilation Office (GMAO) and provides data like wind, temperature, mixing ratio of components, and so on. (Gelaro et al., 2017). In this work, the zonal wind, temperature, air density, surface albedo, water vapor mixing ratio and temperature tendency due to moist process range from 2002 to 2023 are selected. The time resolution is 3-hour per day. The spatial resolution is a  $2.5^\circ \times 2.5^\circ$  latitude-by-longitude grid at 72 model levels from ground to 0.01 hPa.

## 2.4 Singapore radiosonde QBO index

The QBO index employed in this study is derived from Singapore radiosonde measurements obtained by the Meteorological Service Singapore Upper Air Observatory (station 48698;  $1.34^\circ\text{N}$ ,  $103.89^\circ\text{E}$ ; 21 m above mean sea level). The monthly mean zonal wind data processed by the National Aeronautics and Space Administration/Goddard Space Flight Center (NASA/GSFC) is selected, spanning 2002–2023 at pressure levels between 100 hPa and 10 hPa.

## 159 2.5 Water vapor radiative heating rate calculation

160 Troposphere heating by water vapor absorption of near-infrared radiation is an important excitation source for DW1 (Hagan,  
161 1996; Lieberman et al., 2003). Due to the SABER's observational gap in the troposphere, the MERRA-2 dataset is adopted.  
162 In this dataset, temperature, air density, surface albedo, cloud fraction and water vapor mixing ratio (specific humidity) are the  
163 variables necessary for the calculation. The heating rate is the sum of clear sky and cloudy sky (Groves et al., 1982):

$$164 \quad J = (1 - k)J_{clear} + kJ_{cloudy} \quad (1)$$

165 where  $k$  is the cloud fraction,  $J_{clear}$  and  $J_{cloudy}$  are the heating rates of the clear sky and cloudy sky. The calculation equations  
166 for clear sky and cloudy sky are given in Appendix A.

## 167 2.6 Ozone radiative heating rate calculation

168 The calculation of ozone radiative heating follows the Strobel/Zhu scheme (Strobel, 1978; Zhu, 1994), in which the total  
169 heating rate is obtained as the sum of contributions from the Hartley, Huggins, and Chappuis bands, with parameterizations  
170 from Zhu (1994). The required ozone volume mixing ratio (VMR) and density are taken from the SABER L2A dataset. Ozone  
171 VMR is retrieved from vertical emission profiles at 9.6  $\mu\text{m}$  and 1.27  $\mu\text{m}$  (Smith et al., 2013). The former covers all local times  
172 and the latter is limited to daytime. In this study, the 9.6  $\mu\text{m}$  retrievals are used. It should be noted that the Strobel/Zhu model  
173 omits the dominant nighttime chemical-heating source between  $\sim 70$  and 100 km (Zhu, 1994; Xu et al., 2010). Consequently,  
174 the present analysis is restricted to the sum of the three-band heating rates between 20 and 70 km.

## 175 2.7 Method for extracting DW1 and data processing

176 Non-uniform SABER observational data were processed into zonal mean data and used to extract tides. The procedures are  
177 [briefly](#) introduced ~~briefly~~ as follows. Firstly, the kinetic temperature, ozone mixing ratio and ozone radiative heating rate  
178 profiles are interpolated vertically with a 1 km spacing. Profiles ~~of~~ [for](#) each day are sorted into ascending and descending  
179 groups. Secondly, the global temperature and ozone observations at whole heights and in both groups were processed into  
180 zonal mean results, covering latitudes from 50°S to 50°N with a resolution of 5°. At a fixed latitude and height, the following  
181 equation proposed by Xu et al. (2007) is used to extract the tide from the zonal mean temperature in a 60-day window:

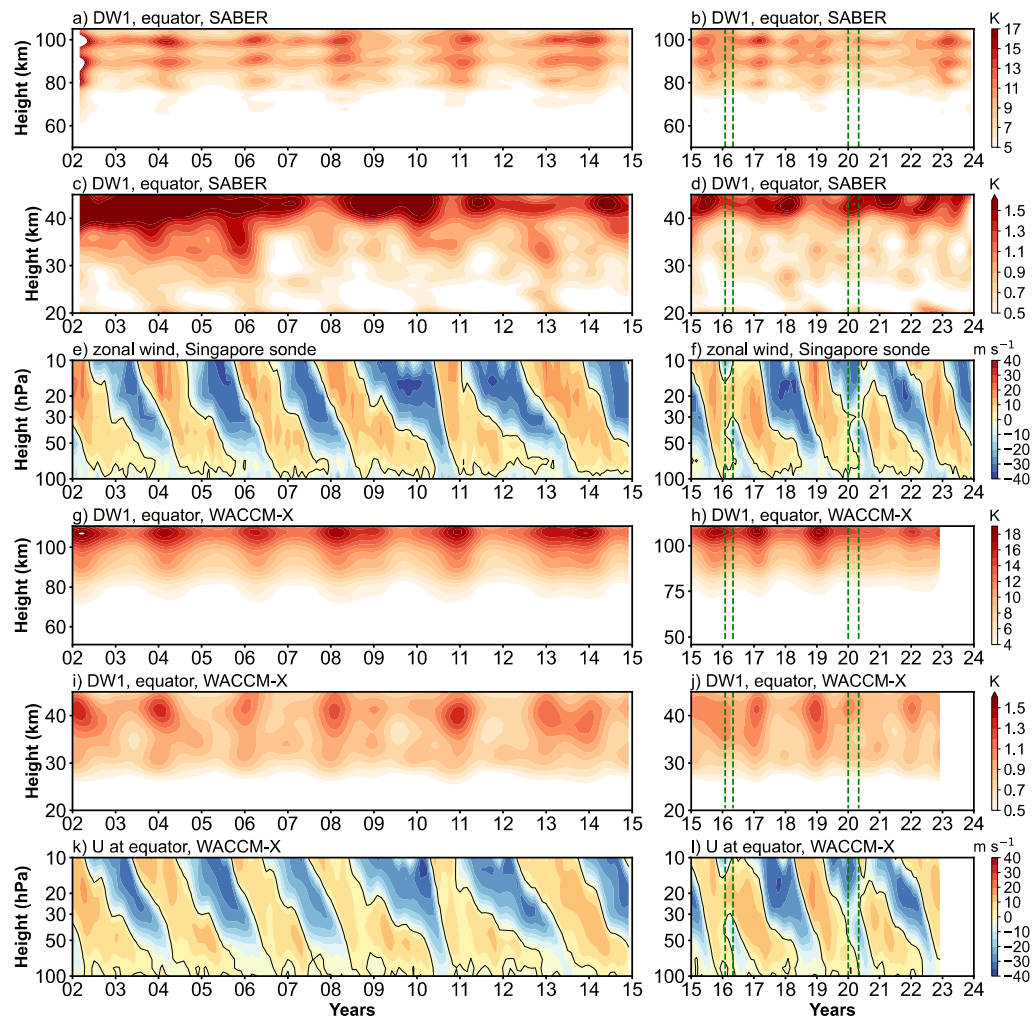
$$182 \quad \frac{1}{2\pi} \int_0^{2\pi} T(t_{LT}, \lambda) d\lambda = \bar{T} + \eta(t - t_0) + \sum_{n=1}^N A_n \cos(n\omega t_{LT}) + \sum_{n=1}^N B_n \sin(n\omega t_{LT}) \quad (2)$$

183 where  $\omega = 2\pi/24(\text{hour})$ ,  $t_{LT}$  is the local time,  $\lambda$  is longitude in radians.  $\bar{T}$  is the 60-day window average of the zonal mean  
184 temperature.  $\eta$  describes the linear trend variation in the window.  $t$  is the day of the window and  $t_0$  is the center day of  
185 the window. The third and fourth terms [of](#) the right section of the equation denotes the superimposed harmonic signals by four  
186 periods migrating tides, including diurnal tide (DW1), semidiurnal tide (SW2), terdiurnal tide (TW3), and 6-h tide (QW4).  $N$   
187 in the third term represents four signals and  $n$  denotes each signal. The amplitude and phase of each migrating tide are retrieved  
188 using  $\sqrt{A_n^2 + B_n^2}$  and  $\arctan(B_n/A_n)$ , respectively. The overlapping analyses are obtained by sliding the 60-day window

189 forward in 1-day intervals to obtain the daily values of the wave characteristics. The details of the methods used for data  
190 processing and tide extraction could refer to Xu et al. (2007, 2009) and Liu et al. (2024a).

191 The method for extracting tidal components from ozone heating rates follows Equation 4 in Xu et al. (2010). The methods for  
192 tidal extraction from MERRA-2 and SD-WACCM-X differ from those used for SABER due to differences in data structure.  
193 Unlike SABER, both MERRA-2 and SD-WACCM-X provide spatially uniform data with a 3-hour temporal resolution. As a  
194 result, a two-dimensional Fast Fourier Transform (2D-FFT) is directly applied to extract daily DW1 amplitudes and phases of  
195 temperature, water vapor heating rate, and temperature tendency due to moist processes. For ~~the~~ further analysis, the Hough  
196 mode decomposition is applied to the DW1. The program is retrieved from [https://github.com/masaru-kogure/Hough\\_Function](https://github.com/masaru-kogure/Hough_Function).  
197 As in Sakazaki (2013), DW1 in the stratosphere can be reasonably well represented by a superposition of only a few ( $\sim 4$ )  
198 Hough modes. Here the (1, -2), (1, -1), (1, 1) and (1, 2) modes are used. The monthly mean temperature DW1 amplitudes  
199 obtained from SABER, MERRA-2 and SD-WACCM-X are calculated. Due to the observational gap of SABER, the  
200 Generalized Lomb-Scargle Periodogram (from PyAstronomy) is applied to fill the missing data of ozone heating rate. A low-  
201 pass Butterworth filter of 3rd order with a cut-off period of 13 months ( $\approx 0.077$  cycles month<sup>-1</sup>) is applied to reveal the DW1  
202 QBO variations (temperature, ozone heating and so on).





205  
206 **Figure 1. (a, b) Low-pass filtered amplitudes (periods longer than 13 months) of the migrating diurnal tide (DW1; monthly mean,**  
207 **in K) as a function of altitude in the mesosphere and lower thermosphere (MLT) and time (2002–2023), derived from**  
208 **SABER/TIMED temperature observations. (c, d) Same as (a, b) but for the stratosphere. (e, f) Zonal wind at the stratospheric**  
209 **equator from Singapore sonde. (g–i) Similar to (a–f), but based on SD-WACCM-X simulations. Vertical green dashed lines indicate**  
210 **the QBO disruption periods in 2015/16 (February–May 2016) and 2019/20 (January–May 2020).**

211  
212 Figure 1 presents the amplitude of DW1 after low-pass filtering and the zonal wind observed by the Singapore sonde. Only  
213 amplitude components [with periods](#) longer than 13 months are retained. In the stratosphere, the zonal wind shows alternating  
214 downward propagating westerly wind (positive value in Figure 1e and 1f) and easterly wind (negative value in Figure 1e and



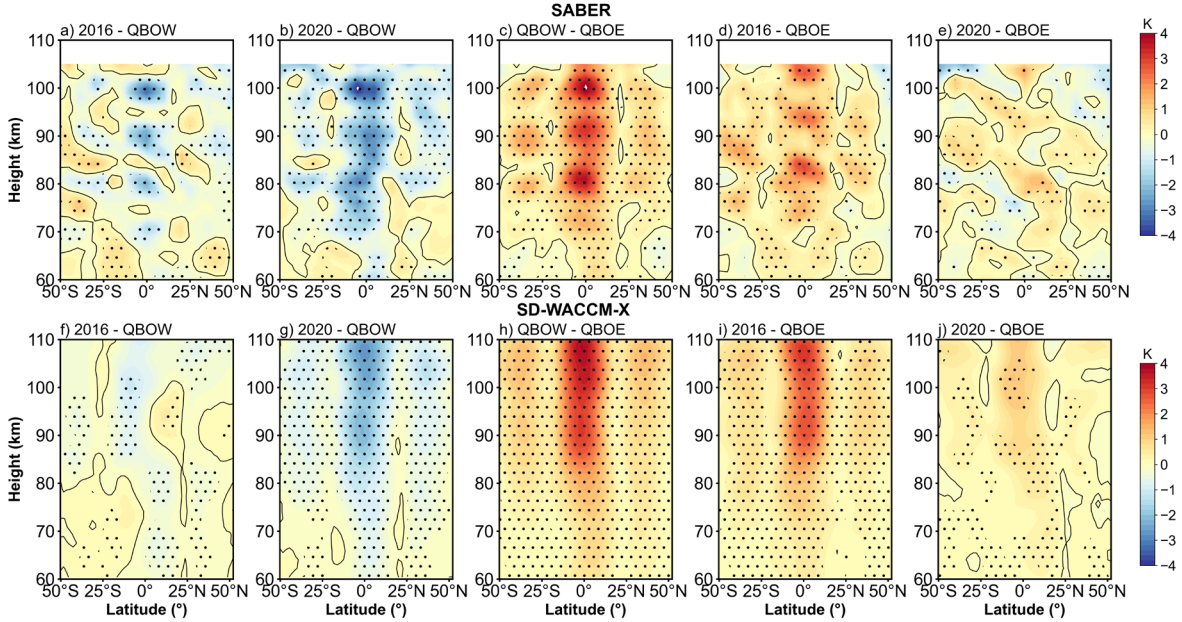
215 1f). Each westerly and easterly transition can be called a QBO cycle. In the stratosphere (Figure 1c and 1d), below 40 km, the  
 216 amplitude of DW1 also shows Quasi-Biennial variability. Above 40 km, the variation ~~becomes~~<sup>is</sup> more complex. This feature  
 217 will be discussed later. In the MLT region (Figure 1a and 1b), the low-pass filtering results of DW1 at the equator exhibit  
 218 Quasi-Biennial variability, with amplitude peaks observed around 90 and 100 km. Comparing the DW1 amplitudes in MLT  
 219 with the zonal wind, the result reveals that the variations in DW1 amplitude correspond to the zonal wind between 20 and 30  
 220 hPa. The amplitude of DW1 is stronger during the QBO westerly wind phase than during the QBO easterly wind phase. This  
 221 result is consistent with Garcia (2023) that the wind fields of QBO at altitudes below 27 km are clearly correlated with the  
 222 DW1 amplitude. Accordingly, in this work, the zonal wind between 20 and 30 hPa is used as the criterion for defining the  
 223 QBO for DW1.

224 During February–May 2016 and January–May 2020, two QBO disruption events occurred (Wang et al., 2023). As shown in  
 225 Figure 1f, the phenomenon ranges from 40 to 15 hPa in 2016 and from 40 to 20 hPa in 2020, which is consistent with previous  
 226 work (Anstey et al., 2021; Newman et al., 2016). Notably, the disruption region coincides with the QBO criterion altitude for  
 227 DW1. To evaluate how the DW1 exhibits response~~s~~<sup>s</sup> to the events, the corresponding time intervals are highlighted with vertical  
 228 green dashed lines. In the stratosphere (Figure 1d), within the disruption periods, amplitude enhancements are observed below  
 229 40 km compared to other QBO easterly phases. Similarly, in the MLT region, the DW1 amplitudes show responses to these  
 230 events (Figure 1b). As shown in Figures 1a and 1b, DW1 amplitudes above 70 km are stronger during these disruption events  
 231 than during other QBO easterly phases, though they remain weaker than those observed during the QBO westerly phase. This  
 232 enhancement is particularly evident around 90 and 100 km.

233 SD-WACCM-X simulations reproduce the SABER observations of DW1 remarkably well in response to QBO disruptions. In  
 234 Figures 1a, 1b, 1f, and 1g, both datasets show enhanced amplitudes during the February–May 2016 and January–May 2020  
 235 events. The difference arises in vertical structure and magnitude. Above 70 km, SABER exhibits three distinct DW1 peaks  
 236 near 80, 90, and 100 km, whereas SD-WACCM-X shows a single peak at approximately 108 km. In the stratosphere above  
 237 40 km, both model and observations peak at similar altitudes, but the simulated amplitudes remain weaker than SABER result.  
 238 Below 40 km, the model captures the QBO-modulated DW1 seen in Figures 1c, 1d, 1i, and 1j. These discrepancies likely stem  
 239 from the MERRA-2 nudging applied up to ~50 km in SD-WACCM-X. In this nudged region, DW1 comprises both propagating  
 240 and non-propagating components (Garcia, 2023; Chapman & Lindzen, 1970). Sakazaki et al. (2018) showed that MERRA-2  
 241 may underestimate the contribution of the non-propagation mode of DW1 (Figure 4 in that work). This feature may explain  
 242 why the amplitude of DW1 is lower than that in SABER and the complex variation of SABER above 40 km.

243 To assess the DW1 response to QBO disruption events over a broad latitude range, the differences between QBO disruption  
 244 and regular QBO easterly and westerly ~~phases~~<sup>phases</sup> are calculated. The DW1 amplitudes used ~~is~~<sup>are</sup> the result after 13 months low-  
 245 pass filtering. Since the DW1 amplitudes typically peak between February and April each year (e.g., Xu et al., 2009; Mukhtarov  
 246 et al., 2009; Garcia, 2023), only the amplitudes during these three months are considered. The classification method for  
 247 different QBO phases is as follows. Regular QBO phases were classified ~~using~~<sup>as</sup> the following method. QBO westerly phase  
 248 (QBOW): February–April zonal wind at 20 hPa is continuously westerly, or zonal wind at 30 hPa is westerly while 20 hPa

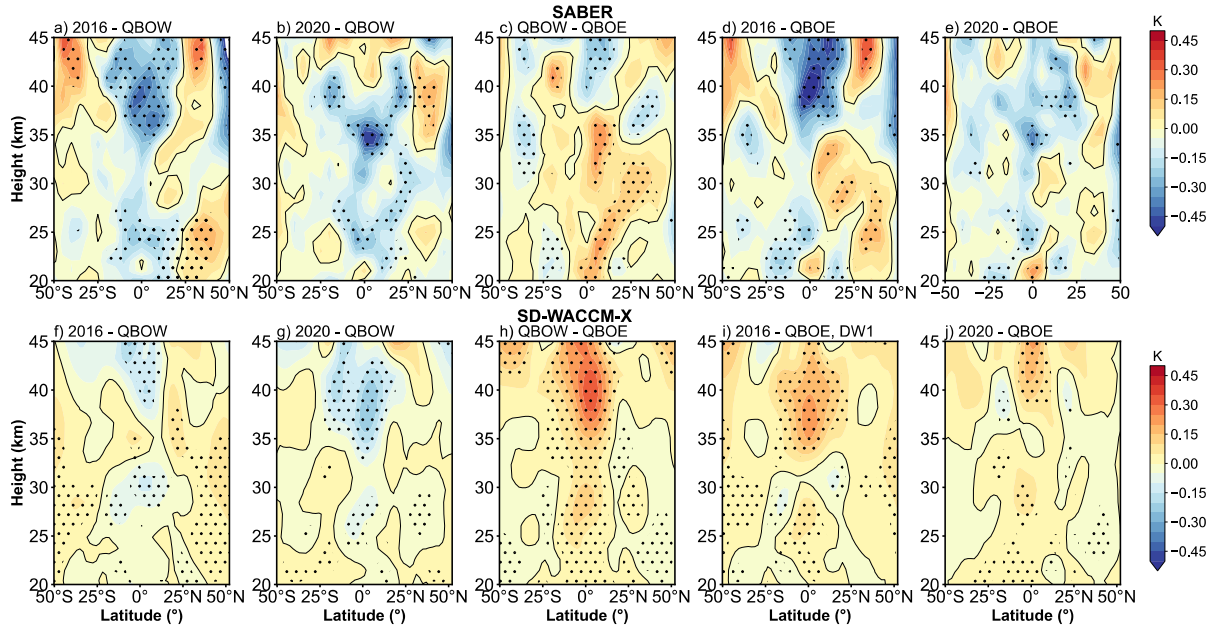
249 undergoes an easterly-to-westerly transition. Easterly phase (QBOE): any remaining cases. The selection of regular QBO  
 250 phases is limited to data from 2002 to 2014, as QBO disruption events occurred after 2015. Additionally, since observations  
 251 in 2002 are mainly available from March to April, data from this year are excluded. The years 2004, 2006, 2008, 2011, 2013,  
 252 and 2014 are classified as QBOW; 2003, 2005, 2007, 2009, 2010, and 2012 as QBOE. For each phase, all filtered amplitudes  
 253 across the selected months are averaged, while processing [data for](#) 2016 and 2020 separately. This approach enables a direct  
 254 comparison of DW1 amplitude anomalies in both latitude and altitude between disruption and regular QBO conditions.  
 255



256  
 257 **Figure 2. Amplitude differences of the DW1 after low-pass filtering between different QBO phases in the mesosphere and lower**  
 258 **thermosphere (MLT) as a function of latitude and altitude. The difference is based on the average from February to April. (a-e) are**  
 259 **corresponding to the difference from the 2016 disruption event minus QBO westerly phases (2016-QBOW), 2020 disruption event**  
 260 **minus QBO westerly (2020-QBOW), QBO westerly minus QBO easterly (QBOW-QBOE), 2016 disruption event minus QBO**  
 261 **easterly (2016-QBOE) and 2020 disruption event minus QBO easterly (2020-QBOE). (f-j) is similar to (a-e) but for SD-WACCM-X**  
 262 **simulation result. The black lines indicate the zero lines. The dotted areas indicate the differences that are significant at the 95%**  
 263 **confidence level.**

264  
 265 Figure 2 gives the difference in DW1 amplitudes during various QBO phases in the MLT region. The significance of the  
 266 differences was assessed using Welch's t-test, and values exceeding the 95 % confidence threshold are highlighted by [in](#) dotted.  
 267 The five columns correspond to the 2016 disruption event minus QBO westerly (2016-QBOW), 2020 disruption event minus  
 268 QBO westerly (2020-QBOW), QBO westerly minus QBO easterly (QBOW-QBOE), 2016 disruption event minus QBO  
 269 easterly (2016-QBOE) and 2020 disruption event minus QBO easterly (2020-QBOE), respectively. The relative change

270 between different QBO phases is also calculated (e.g.,  $\frac{QBOW-QBOE}{QBOE}$ , and so on). The comparison between QBOW and QBOE  
 271 (Figure 2c) reveals that DW1 amplitudes are significantly larger during QBOW, particularly at the equator and around 30°N/S  
 272 above ~75 km. The enhancements reach ~2.79 K (~34.5 %) at the equator and ~0.79 K (~20.6 %) at 30°N/S, with peak values  
 273 as high as ~3.30 K (~38.5 %) and ~1.19 K (~31.7 %) at respective latitudes. During the 2016 disruption (Figures 2a, 2d), DW1  
 274 amplitudes lie between QBOE and QBOW values. The clear enhancement could be found from 75 km to 105 km. The pattern  
 275 in 2016–QBOE closely resembles that of QBOW–QBOE, although the equatorial peaks appear at slightly higher altitudes.  
 276 The enhancements reach ~1.56 K (~20.5 %) at the equator and ~0.54 K (~14.4 %) at 30°N/S. The peak enhancements relative  
 277 to QBOE reach ~2.40 K (~26.5 %) at the equator and ~0.87 K (~29.5 %) at 30°N/S. Compared to QBOW, however, the  
 278 ~~equatorial~~ difference drops to -2.28 K (-18.8 %) at equator and ~0.12 K (4.6 %) at 30°N/S. In contrast, the 2020 disruption  
 279 event shows weaker amplitude increases relative to QBOE (Figures 2b, 2e). The clear enhancement occurs from 75 km to 90  
 280 km. The increment reaches ~0.50 K (~6.0 %) at the equator and ~0.26 K (~7.7 %) at 30°N/S, with a peak enhancement of only  
 281 ~0.91 K (~11.6 %) at the equator and ~0.31 K (~14.2 %) at 30°N/S. Compared to QBOW, the difference is -2.3 K (~-21.1%)  
 282 at the equator and -0.57 K (~-12.0 %) at 30°N/S. These values are considerably lower than those observed during the 2016  
 283 event or the typical QBOW enhancement. The SD-WACCM-X model reproduces the general features described above  
 284 (Figures 2f–2j), though the vertical structure of the simulated amplitudes differs slightly from observations.



286  
 287 **Figure 3. Similar to figure 2 but in stratosphere. (a-e) give the difference result derived from SABER. (f-g) give the difference result**  
 288 **derived from SD-WACCM-X.**

289

Figure 3 compares the stratospheric DW1 amplitude differences derived from the SABER dataset and SD-WACCM-X simulations. The enhancement pattern resembles that seen in the MLT region but is confined to tropical latitudes. Because SABER exhibits complex variability above 40 km, the analysis is restricted to altitudes below that level. As shown in Figure 3c, the DW1 amplitudes during QBOW exceed those during the QBOE by  $\sim 0.21$  K ( $\sim 37.9\%$ ) at around 20–25 and 30–35 km. In SD-WACCM-X result (Figure 3h), the positive peaks are found at 25–30 km and 35–40 km, which is  $\sim 0.21$  K ( $\sim 27.4\%$ ). The amplitudes during the disruption events are much weaker relative to ~~that~~ those during QBOW phases shown in both datasets (Figure 3a, 3b, 3f and 3g). Compared to ~~the~~ QBOE, the strengthening during the 2016 QBO disruption event occurs at approximately 30–35 km in SABER (Figure 3d) and 35–45 km in SD-WACCM-X (Figure 3i), which is  $\sim 0.15$  K ( $\sim 21.8\%$ ) and  $0.20$  K ( $\sim 23.9\%$ ), respectively. During the 2020 event, the amplitudes are comparable to those during ~~relative to the~~ QBOE (Figure 3e and 3j).

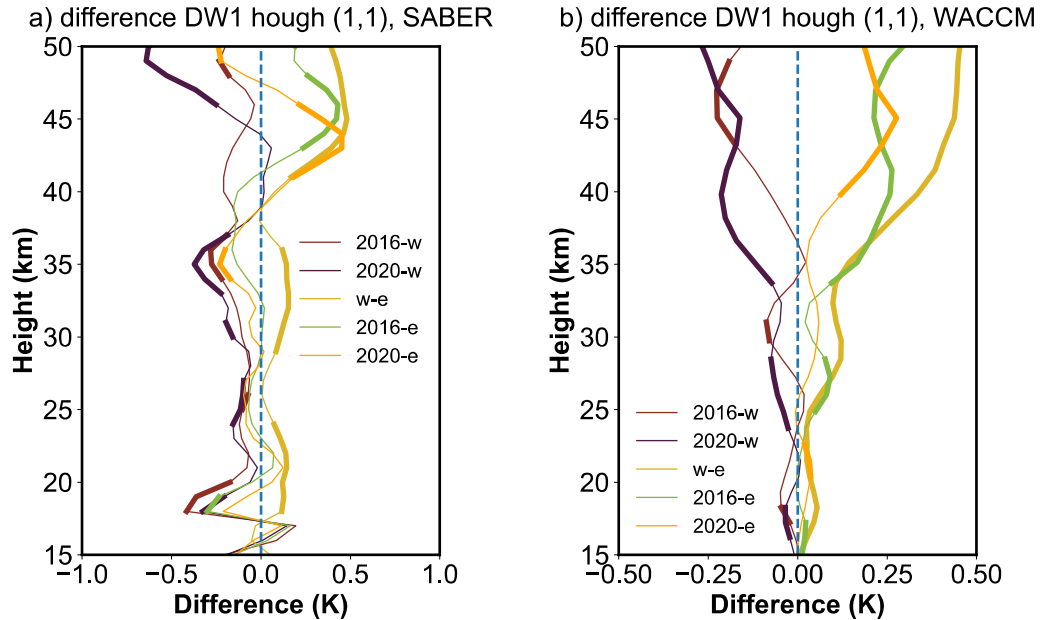


**Figure 4. Amplitude differences profiles of the DW1 (1, 1) mode after low-pass filtering between different QBO phases in the stratosphere like Figure 2. (a) gives the difference result derived from SABER. (b) give the difference result derived from SD-WACCM-X. The bold lines indicate the differences that are significant at the 95% confidence level.**

Figure S2-C2 presents the low-pass time series of the equatorial DW1 amplitude and the (1,1) mode amplitude at 95 km, showing that the (1,1) mode closely follows the equatorial DW1 amplitude. In the stratosphere, however, the superposition of propagating tides and trapped modes complicates the interpretation. To separate these contributions, Figure S1-C1 compares the amplitudes of the (1,1) and (1, -2) modes under different QBO phases. The trapped mode is dominant below 60 km, while the (1,1) mode is relatively weaker. A clear distinction between QBOW and QBOE is evident in the (1,1) mode (Fig. S1a-C1a), whereas the (1, -2) mode shows little difference between the phases. Together, Figures S1-C1 and S2-C2 indicate that the (1,1)

311 mode captures nearly all of the QBO-related variability in the MLT region, motivating a closer examination of ~~the (1,1)~~  
312 mode in the stratosphere.  
313 Figure 4 shows the vertical profiles of amplitude differences in the DW1 (1,1) mode between QBO phases after low-pass  
314 filtering. The bold lines denote differences significant at the 95% confidence level. In SABER observations (Fig. 4a),  
315 amplitudes during QBOW exceed those in QBOE throughout 20–45 km. During the 2016 and 2020 events, amplitudes remain  
316 close to ~~those in~~ QBOE between 20–40 km but become stronger above 40 km, with maximum differences of ~~~-0.15 (~11 %),~~  
317 ~~-0.18 (~12 %),~~ ~0.36 K (~36 %), ~0.21 K (~21 %), and ~0.18 K (~17 %) for ~~2016-QBOW, 2020-QBOW,~~ QBOW–QBOE,  
318 2016 – QBOE, and 2020–QBOE, respectively. WACCM-X simulations (Fig. 4b) reproduce a similar vertical pattern: during  
319 the disruption events, amplitudes lie between QBOE and QBOW values in the 20–50 km region.

### 320 3.2 DW1 phases response to QBO disruption events

321 In this section, whether the DW1 phases and wavelengths respond to QBO disruptions will be analysed. As discussed above,  
322 the DW1 QBO variability is mainly in (1, 1) mode. Hence, ~~we focus on~~ the phase of (1, 1) mode ~~is focused~~. As noted previously,  
323 the pronounced DW1 amplitude observed from February to April renders the phase during this period an important variable.  
324 Hence, the statistics ~~s are~~ ~~is~~ based on these periods. ~~Due to~~ ~~Since~~ the phase values change ~~cyclically~~ (e.g., it jumps from  $\pi$  to  $-\pi$ ),  
325 causing the overestimation of the standard deviation. We apply the ~~following~~ method ~~following~~. ~~We first~~  
326 ~~calculate~~ ~~Calculate~~ averages and standard ~~deviation~~ ~~devotion~~ (or error) of sine and cosine Fourier components ~~first~~, and then  
327 calculate the average phase and its ~~confidence~~ ~~confidential~~ interval using ~~the~~ error propagation. The mean value and its 95%  
328 ~~confidence~~ ~~confidential~~ interval in different QBO phases (listed in section 3.1) are calculated. The statistical results for the  
329 phases in 2016 and 2020 are calculated separately.

330

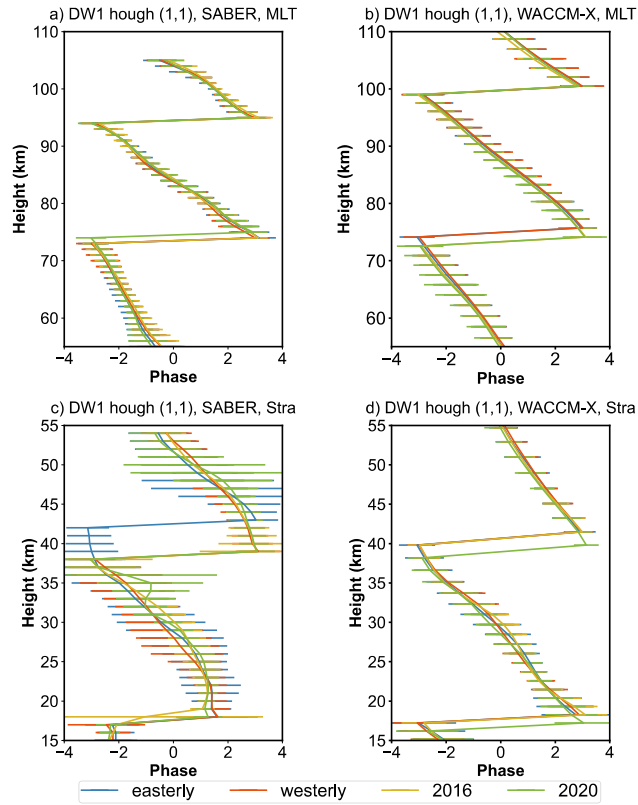


**Figure 5. The DW1 (1, 1) mode vertical phase structure in mesosphere and lower thermosphere (MLT) and stratosphere averaged from February to April during QBO westerly phase (orange), QBO easterly phase (blue), 2016 QBO disruption event (yellow) and 2020 QBO disruption event (green). (a, c) give the SABER observation result. (b, d) give the WACCM-X simulations. The error bar denotes the 95% confidence interval of the phases for each height.**

Figure 5 illustrates the vertical phase structure of DW1 (1, 1) mode in the mesosphere and lower thermosphere (MLT) and stratospheric regions, respectively, averaged over the February–April period. The results are presented for various QBO phases at different latitudes, based on data from (a, c) SABER and (b, d) SD-WACCM-X. Error bars indicate the 95% confidence interval of the phase average. The lines represent different QBO phases and events: QBO westerly phase (orange), QBO easterly phase (blue), the 2016 QBO disruption event (yellow), and the 2020 QBO disruption event (green).

In the MLT region (Figure 5a and 5b), the vertical phase profiles exhibit minimal differences across the QBO westerly, easterly and 2016 phases. The structures are nearly identical in both the simulations and observations, with two phase peaks (approximately  $\pi$  rad) consistently present. The peak altitudes remain almost unchanged among the different QBO phases, suggesting a limited phase response to QBO disruption events in the MLT region. During the 2020 event, the phase peaks at around 75 km is higher than that during other QBO phases in SABER and lower than that in WACCM-X.



348 The DW1 vertical phase structures in the stratosphere region are given in Figure 5c and 5d. In SABER observations, there ~~is~~  
349 are clear differences between QBOW and QBOE. The phase peaks (at around 40 km) during the QBOW ~~locate~~occur about 3  
350 km lower than those during QBOE ~~about 3 km~~. During the QBO disruption events, the phase structure is similar to that during  
351 the QBOW. From WACCM-X simulations, the feature is similar to the pattern in MLT (Figure 5b). During the 2020 disruption  
352 event, the phase ~~reach~~ peaks are lower than other QBO phases by about 1 km.

353 The phase peaks described above ( $\sim\pi$  rad) are used to calculate the DW1 wavelengths in both the stratosphere and MLT regions.  
354 The altitude difference between the two peaks is taken as the wavelength, following the method of Liu et al. (2021). The  
355 statistical results of DW1 (1, 1) mode wavelengths under different QBO phases are summarized in Table 1, which lists the  
356 mean values and standard deviations at various altitudes. In the MLT region, the mean wavelengths are  $\sim 21$  km in the SABER  
357 dataset and  $\sim 25$  km in the SD-WACCM-X dataset. The wavelengths during QBO disruption events are comparable to those  
358 during the QBO westerly and easterly phases, a feature also captured in the SD-WACCM-X simulations. In the mesosphere,  
359 the mean wavelengths are  $\sim 34$  km in SD-WACCM-X and  $\sim 33$  km in SABER. In this region, there are clear differences between  
360 QBOW and QBOE. The QBOE wavelength is about 2 km shorter than that during QBOW ~~about 2 km~~. In the stratosphere, the  
361 QBOE wavelength is about 2 km longer than that during QBOW ~~about 2 km~~. The wavelengths during the QBO disruptions  
362 are close to those ~~that~~ during QBOW.

363 According to the theoretical framework proposed by Forbes and Vincent (1989) and Kogure and Liu (2021), zonal winds  
364 modify the intrinsic frequency of tides through Doppler shifting, thereby altering their vertical wavelengths. Specifically,  
365 westerly winds lead to longer DW1 vertical wavelengths, whereas easterly winds result in shorter ones. However, the  
366 dependence shown in Table 1 differs from that reported in previous studies. This discrepancy can be attributed to differences  
367 in methodology. In this study, the vertical wavelengths are determined from the phase difference between adjacent peaks ( $+\pi$ ).  
368 In the stratosphere, one of these peaks typically occurs in the lower stratosphere ( $\sim 18$  km) and the other in the upper  
369 stratosphere ( $\sim 40$  km). Consequently, the estimated wavelengths encompass the combined influences of both the QBO and  
370 SAO, producing a mixed result that deviates from earlier findings

371

372 **Table 1. The comparison of mean (left of the slash) and standard deviations (right of the slash) of DW1 (1, 1) mode wavelengths (in**  
373 **km) revealed by SD-WACCM-X and SABER from 15 km to 105 km between QBO westerly phase, easterly phase, 2016 disruption**  
374 **event and 2020 disruption event calculated from February to April.**

Data	SD-WACCM-X			SABER		
altitude	$\sim 15$ km – $\sim 40$ km	$\sim 40$ km – $\sim 75$ km	$\sim 75$ km – $\sim 105$ km	$\sim 15$ km – $\sim 40$ km	$\sim 40$ km – $\sim 75$ km	$\sim 75$ km – $\sim 105$ km
Westerly	22.97/1.49	34.47/1.79	25.10/1.84	21.81/1.44	33.12/1.78	21.29/1.04
Easterly	22.51/1.73	34.42/2.15	25.60/2.20	24.46/1.99	30.84/2.35	20.56/1.30



2016	22.56/1/33	33.26/1.58	25.58/2.03	21.48/2.31	33.32/2.10	21.28/0.85
2020	22.71/1.87	33.80/2.68	26.27/2.41	21.08/1.77	34.24/1.46	20.39/1.35

375

## 376 4 Discussion

377 In this section, we discuss how the QBO disruptions modulate the DW1 by several mechanisms from the lower atmosphere to  
378 the upper atmosphere. As in Introduction, three primary mechanisms are considered: background zonal wind and its latitudinal  
379 shear (e.g., Forbes and Vincent, 1989; Hagan et al., 1999; McLandress, 2002b); diurnal heating (McLandress, 2002b; Riggin  
380 and Lieberman, 2013; Ortland, 2017); tide–gravity wave (GW) interactions (Mayr et al., 1998; McLandress, 2002a; Lu et al.,  
381 2012; Wang et al., 2024). The mechanism analysis will be organized by tidal heating (troposphere and stratosphere), the  
382 dissipation and tidal propagation (from stratosphere to mesosphere) and tide-gravity wave interaction (mesosphere and lower  
383 thermosphere).

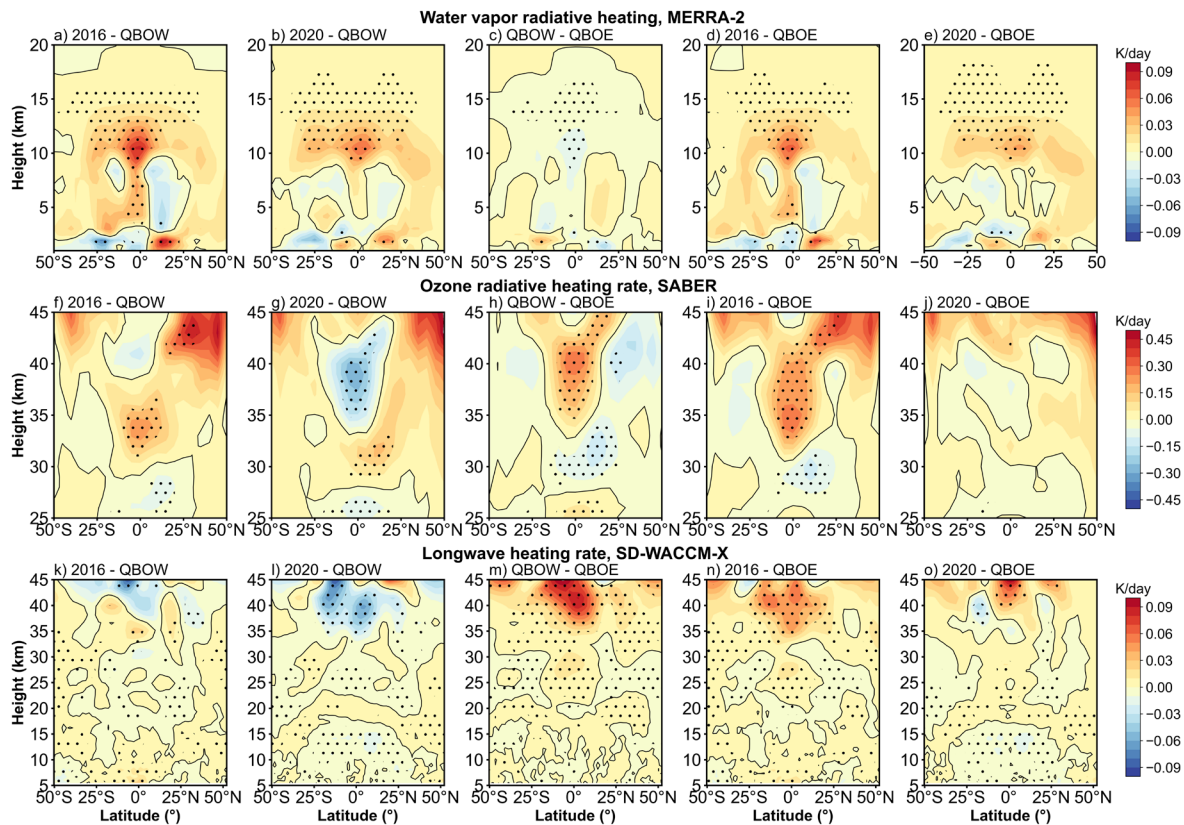
### 384 4.1 Tidal heating variation during the QBO disruption events

385 ~~The influence of QBO disruption events on DW1 can be traced back to its excitation mechanisms.~~ The excitation sources of  
386 DW1 can be broadly classified into three categories: (1) solar radiation in the near-infrared (IR) absorbed by tropospheric H<sub>2</sub>O,  
387 (2) solar radiation in the ultraviolet (UV) absorbed by stratospheric and lower mesospheric O<sub>3</sub>, and (3) solar radiation absorbed  
388 by O<sub>2</sub> in the Schumann–Runge bands and continuum (Hagan, 1996). Additionally, Kogure and Liu (2021)  
389 highlighted~~suggested~~ the role of latent heating in modulating DW1. It is worth noting that the timing of the 2016 QBO  
390 disruption event coincides with the phase of the extreme El Niño (e.g., Santoso et al., 2017; Hu and Fedorov, 2017). El Niño  
391 itself could modulate the DW1 (Kogure and Liu, 2021). Attention should be paid to the contribution of water vapor and latent  
392 heating jointly influenced by QBO disruption and 2015/16 extreme El Niño. Overall, this section focuses on examining the  
393 effects of water vapor radiative heating, ozone radiative heating, and latent heating on DW1.

394 ~~It is worth noting that the timing of the 2016 QBO disruption event coincides with the phase of the extreme El Niño (e.g.,~~  
395 ~~Santoso et al., 2017; Hu and Fedorov, 2017). El Niño itself could modulate the DW1 (Kogure and Liu, 2021). The contribution~~  
396 ~~of water vapor and latent heating should be also paid attention.~~

397 ~~During the 2016 QBO disruption, which coincided with the strong 2015/2016 El Niño, the two phenomena jointly modulated~~  
398 ~~the DW1 heating sources. El Niño enhances moisture anomalies that increased with altitude, culminating in pronounced~~  
399 ~~positive signals in the upper troposphere and lower stratosphere (UTLS) (Johnston et al., 2022). In contrast, the occurrence of~~  
400 ~~2016 QBO disruption introduces a shear transition from westerly to easterly near 40 hPa, which strengthens tropical upwelling~~  
401 ~~and lowers cold point temperatures. This dynamical response injects H<sub>2</sub>O-poor air into the lower stratosphere, partially~~  
402 ~~offsetting the El Niño-driven moistening. The water-vapor concentrations are still above the climatological seasonal cycle~~  
403 ~~under the modulation of these two phenomena (Diallo et al., 2018). Unlike 2016, the 2020 disruption produces only weak~~

404 lower-stratospheric dehydration ( $\sim 2-3\%$ ) because enhanced upwelling and cold-point cooling are suppressed. Instead,  
 405 anomalously warm tropopause temperatures associated with Australian wildfire smoke facilitates significant moistening of the  
 406 lower stratosphere (Diallo et al., 2022).  
 407



408  
 409 **Figure 6.** As in Figure 2 and Figure 3, but the difference of amplitude in DW1 component (after low-filtering) of (a-e) water vapor  
 410 heating rate DW1 component from MERRA-2, (f-j) ozone heating rate DW1 component from SABER and (k-o) longwave heating  
 411 rate from SD-WACCM-X. The dotted areas indicate the differences that are significant at the 95% confidence level.

412  
 413 Figure 6 presents the difference of amplitude in the DW1 component of water vapor radiative heating rate, ozone radiative  
 414 heating rate, and longwave heating rate. The calculation method is consistent with the method described given in Section 3.1.  
 415 During QBOE and QBOW, the DW1 component of water vapor heating remains nearly unchanged (Figure 6c). However,  
 416 during the 2016 QBO disruption (Figures 6a, 6d), a notable enhancement in water vapor heating appears between 10–13 km  
 417 altitude around the equator. The difference between 2016 and QBOE is  $\sim 0.02 \text{ K day}^{-1}$  with increases of  $\sim 2.5\%$  relative to  
 418 QBOW. The difference between 2016 and QBOW is  $0.03 \text{ K day}^{-1}$  with increases of  $\sim 3.7\%$  relative to QBOW. A similar pattern

419 is seen during the 2020 QBO disruption event (Figures 6b and 6e). The relative changes of ~~the~~ regional average ~~increase~~~~rise~~  
420 by ~1.2 % compared to QBOW and ~2.3 % compared to QBOE.

421 Figures 6f–6j reveal that the largest QBO-related differences in the DW1 component of ozone heating occur near the equator  
422 between 30 and 45 km. In QBOW, ozone heating rates between 35 and 45 km exceed those in QBOE by ~2.1 % (Figure 6h).  
423 During the 2016 QBO disruption event (Figures 6f and 6i), ozone radiative heating rates are ~3.6 % larger than those in the  
424 QBOW between 30 and 35 km and ~2.9 % larger than those in the QBOE within the 30–40 km range. In contrast, during the  
425 2020 disruption event (Figures 6g and 6j), the ozone heating rate is comparable to that of the easterly phase and lower than  
426 that of the westerly phase in the 35–45 km altitude range.

427 In the SD-WACCM-X simulation, the longwave heating rate accounts for the effects of three major absorbers: H<sub>2</sub>O, CO<sub>2</sub>, and  
428 O<sub>3</sub> (Neale et al., 2010). This parameter could be used to verify the effect of the water vapor and ozone radiative heating. The  
429 DW1 component of the longwave heating rate from SD-WACCM-X is shown in Figures 6k–6o. The heating rate difference  
430 between the QBOW and QBOE reveals a positive peak at 40 km near the equator, with no significant difference at the  
431 equatorial tropopause (Figure 6m). The feature corresponds to the observed pattern (Figures 6c and 6h). In the 2016 disruption  
432 case, the simulated equatorial heating rate exhibits positive peaks around 35 km and 15 km (not significant), aligning well with  
433 observations in terms of altitude (Figure 6k and 6n). In the 2020 disruption case, the simulation (Figure 6l and 6o) agrees with  
434 the observed stratospheric heating features (Figures 6g and 6j). However, at around 15 km, the simulation shows negative  
435 peaks near the tropopause, whereas the observations indicate positive peaks (Figures 6b and 6e). As longwave heating  
436 incorporates contributions from multiple absorbers, the discrepancies may be attributed to the influence of other constituents.

437 As discussed above, the (1,1) Hough mode captures nearly all QBO-related variability in the MLT. Accordingly, the (1,1)  
438 component of the ozone heating rate ~~are~~~~is~~ extracted for diagnosis. Numerous studies have noted that the vertical thickness of  
439 ozone heating (~40 km) is large compared with the relatively short vertical wavelength of the DW1, implying weak projection  
440 onto the (1,1) and thus limited excitation efficiency (e.g., Chapman and Lindzen, 1970; Hagan, 1999; Garcia, 2023). Studies  
441 with GSWM and the Tide Mean Assimilation Technique (TAMT) further indicate that DW1 forced by ozone heating tends to  
442 be out of phase with DW1 forced by water-vapor heating, reducing the amplitudes (Hagan, 1996; Ortland et al., 2017).  
443 Consistent with this mechanism, MLS observations show a pronounced depression of the tropical diurnal tide near 1.0 hPa  
444 (~49.5 km; Wu et al., 1998), which may ~~be attributed~~~~attribute~~ to interference between the upward-propagating (1,1) tide and  
445 a locally forced component from ozone heating. Figure 7 compares DW1 (1,1) temperature and ozone heating rate between  
446 different QBO phases and shows ~~a~~ suppressed (1,1) amplitudes feature around ~50 km, while ozone heating peaks slightly  
447 below this level. This feature aligns with the MLS evidence. Therefore, the ozone may not play ~~a~~ positive role for the DW1  
448 (1, 1) mode. Whether ~~the~~ ozone heating modulated DW1 (1, 1) mode ~~requires~~~~there needs~~ more detailed investigation like  
449 model simulation from Kogure et al. (2023).

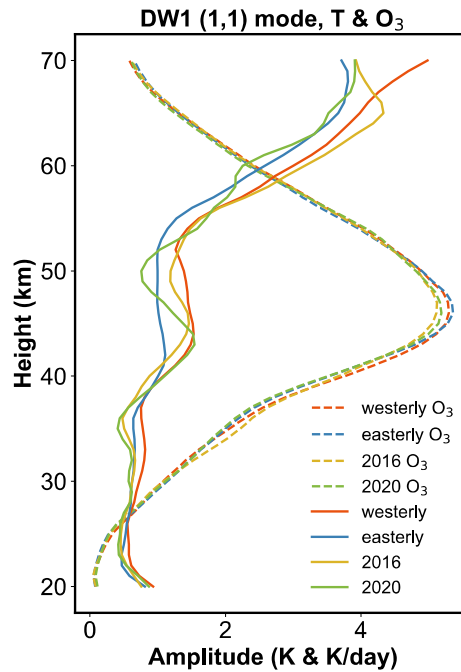
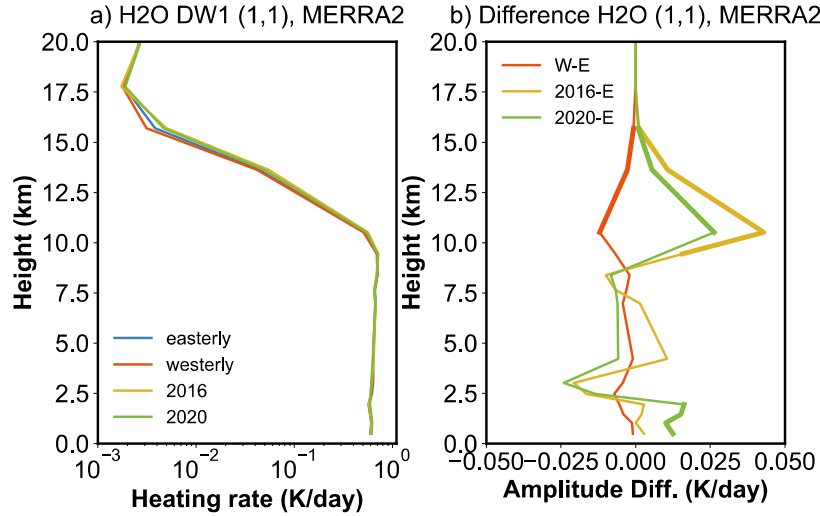


**Figure 7. The comparison between the temperature and heating rate of the DW1 (1, 1) mode between different QBO phases ~~and~~ their differences.**

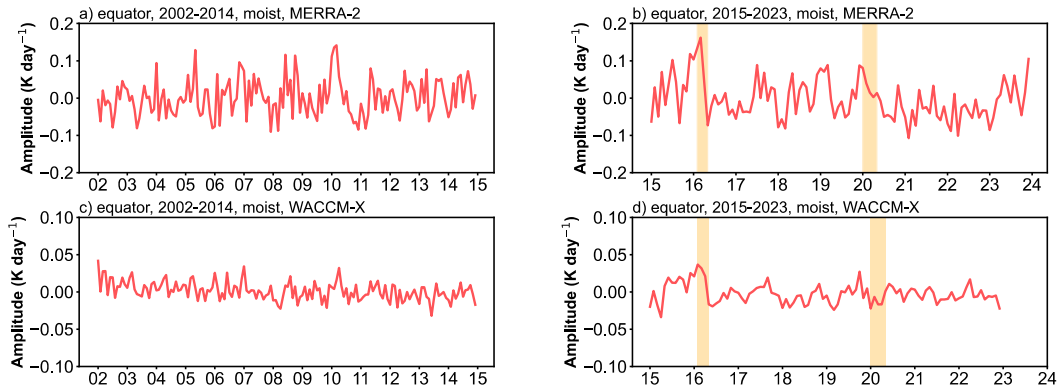
The DW1 (1,1) mode is primarily excited by water-vapor heating (Forbes and Garrett, 1978). As shown in equation A1 and A10 in Appendix A, the concentration of water vapor is one of the key factors controlling water vapor radiation. During the 2016 QBO disruption, which coincided with the strong 2015/2016 El Niño, the two phenomena jointly modulated the DW1 water vapor heating sources. El Niño enhances moisture anomalies that increase with altitude, culminating in pronounced positive signals in the upper troposphere and lower stratosphere (UTLS) (Johnston et al., 2022). In contrast, the occurrence of the 2016 QBO disruption introduces a shear transition from westerly to easterly near 40 hPa, which strengthens tropical upwelling and lowers cold-point temperatures. This dynamical response injects H<sub>2</sub>O-poor air into the lower stratosphere, partially offsetting the El Niño-driven moistening. The water vapor concentrations remain above the climatological seasonal cycle under the modulation of these two phenomena (Diallo et al., 2018). Unlike 2016, the 2020 disruption produces only weak lower-stratospheric dehydration (~2–3 %) because enhanced upwelling and cold-point cooling are suppressed. Instead, anomalously warm tropopause temperatures associated with Australian wildfire smoke facilitate significant moistening of the lower stratosphere (Diallo et al., 2022). It is foreseeable that the increase in water vapor concentration modulated by QBO disruptions and 2015/16 El Niño event will lead to an increase in the radiative heating rate of water vapor.

Figure 8 presents the water vapor radiative heating rate profiles of the DW1 (1,1) mode for different QBO phases and their differences. The heating rate exhibits large values in the troposphere, extending up to ~10 km. The average magnitude could reach ~0.62 K day<sup>-1</sup>. During the 2016 QBO disruption event (Fig. 8b), the maximum difference occurs at 10.5 km, reaching

0.043 K day<sup>-1</sup>, which represents an ~8 % increase relative to QBOE. However, the DW1 amplitude varies by ~20.5 % compared to QBOE, indicating that water-vapor heating accounts for only ~39 % of the observed amplitude difference. This feature suggests that additional mechanisms must be involved. A similar enhancement of water-vapor heating is observed during the 2020 event, with the largest difference again at 10.5 km (~0.026 K day<sup>-1</sup>), corresponding to an ~5 % increase relative to QBOE.



**Figure 8. Heating rate profiles of the DW1 (1, 1) mode between different QBO phases and their differences. (a, b) give the water vapor heating profile and its difference derived from MERRA2. The bold lines indicate the differences that are significant at the 95% confidence level.**



**Figure 9. (a, b) The desseasonalized time series of DW1 amplitudes of latent heating rate (K day<sup>-1</sup>) at equator averaged from 800 hPa to 200 hPa derived from MERRA-2. (c-d) is as in (a-b) but from SD-WACCM-X. The orange-filled areas represent two QBO disruption events.**

Figure 9 shows the deseasonalized time series of the DW1 component of latent heating rate ( $\text{K day}^{-1}$ ) at the equator, averaged from 800 hPa to 200 hPa. In this tropospheric layer, the latent-heating signal shows less differences between QBOW and QBOE phases. Therefore, deseasonalization is directly applied to the full time series without separating the two QBO states. In MERRA-2 and SD-WACCM-X, the anomaly peaks reach  $0.162 \text{ K day}^{-1}$  and  $0.037 \text{ K day}^{-1}$ , respectively, which correspond to increases of about  $\sim 32 \%$  and  $\sim 25 \%$  above their climatological means ( $0.50 \text{ K day}^{-1}$  and  $0.15 \text{ K day}^{-1}$ ). When averaged over the February-April in 2016, the anomalies remain elevated at  $0.11 \text{ K day}^{-1}$  ( $\sim 22 \%$ ) in MERRA-2 and  $0.03 \text{ K day}^{-1}$  ( $\sim 19.2 \%$ ) in SD-WACCM-X. In contrast, during the 2020 QBO disruption event, the amplitudes in both MERRA-2 and SD-WACCM-X remain closer to the climatological means, with deviations of  $0.018 \text{ K day}^{-1}$  and  $-0.013 \text{ K day}^{-1}$ , respectively. These results suggest that latent heating may contribute to the amplification of DW1 amplitudes during the 2016 QBO disruption event but show little effect during the 2020 event.

#### 4.2 ~~Tidal propagation~~Effect of zonal wind and its latitude shear during the events

In this section, we focus on the effects of the background wind on tides during their upward propagation. As discussed in Forbes and Vincent (1989), ~~the (1,1) mode is dissipated more in the easterly wind than in the westerly wind.~~ Zonal zonal winds distort the tidal expansion functions such that they are amplified and broadened in the winter hemisphere ( $U > 0$ ) but are considerably diminished under summer conditions. As shown in Figure 1f, during the 2016 QBO disruption, the westerly wind layer is unusually thick in the stratosphere, though still weaker than in the normal QBOW. - In contrast, during the 2020 event, the westerly wind layer is extremely shallow, essentially indistinguishable from the easterly phase. Thus, the zonal wind in the stratosphere during the 2016 QBO disruption is conducive to the growth of tidal amplitude. During the 2020 QBO disruption event, the influence of zonal winds in the stratosphere on tides is essentially consistent with that observed during the QBOE period.

Additionally, the zonal wind influences the intrinsic frequency through Doppler shifting and therefore modifies the variation of the vertical wavenumber. The increase or decrease of the vertical wavenumber depends on the direction of zonal wind. Under the usual Newton-cooling/Rayleigh-friction parameterizations, the effective dissipation is approximately proportional to the squared local vertical wavenumber (Forbes and Vincent, 1989; Kogure and Liu, 2021). Consequently, zonal wind could also influence the dissipation process. To examine the dissipation during the event, we apply the amplitude ratio method.

As in Forbes and Vincent (1989), the amplitude growth equation is:

$$\frac{A(z)}{A(70)} = \exp \left\{ \int_{70}^z \left[ -k_i + \frac{1}{2H} \right] dz \right\} \quad (3)$$

where  $A$  is the amplitude,  $z$  is the altitude (in km),  $H$  is the local scale height and  $k_i$  is the imaginary part of the complex vertical wavenumber that governs the damping of the amplitude profile. Calculating the ratio of amplitude using Equation (3) during two different QBO phases (e.g., 2016/QBOE) yields:

$$\frac{A_{2016}(z)}{A_{QBOE}(z)} = \exp \left\{ \int_{70}^z - \left( k_{i,2016}(z) - k_{i,QBOE}(z) \right) dz \right\} \quad (4)$$

516 The scale height term is removed, leaving the dissipation term. Thus, the changes in amplitude ratio may reflect tidal dissipation  
517 variations at the altitude.

518 Figure C3 presents the ratio results derived from SABER observations and SD-WACCM-X simulations. In the SABER data  
519 (Figure C3a), during the 2016 event, two distinct peaks appear in the lower stratosphere near 22 km and 30 km when comparing  
520 the disruption events with the QBOE phase (green lines), possibly indicating relatively less dissipation during the 2016 QBO  
521 disruptions. During the 2020 event, the lower peak (~22 km) is close to that during 2016 event, while the upper peak (~30 km)  
522 is relative weak to the 2016 event. This may suggest a relatively large dissipation at those heights. The SD-WACCM-X  
523 simulations reproduce a similar pattern, although the peak altitudes differ slightly. All simulated ratios remain above 1, which  
524 may indicate stronger tidal source activity in the SD-WACCM-X simulations. Overall, these results suggest that during QBO  
525 disruptions, zonal wind may lead to relatively less dissipation processes, thereby affecting DW1 amplitudes.~~During the 2016~~  
526 ~~QBO disruption, the westerly wind layer is unusually thick in stratosphere, though still weaker than in the normal QBOW.~~  
527 ~~Under these conditions, the background wind tend to enhance tidal amplitudes. However, the thinner westerly layer compared~~  
528 ~~with the normal QBOW phase likely contribute to somewhat weaker amplitudes. In contrast, during the 2020 event, the~~  
529 ~~westerly wind layer is extremely shallow, essentially indistinguishable from the easterly phase, so the background wind exerts~~  
530 ~~little or no amplifying effect on tides compare to QBOE.~~

531 In addition to zonal-mean wind effects, latitudinal shear of zonal wind in the subtropical mesosphere can modulate the seasonal  
532 variability of the (1,1) mode (McLandress, 2002b; Mayr and Mengel, 2005; Sakazaki et al., 2013; Kogure et al., 2021; Siddiqui  
533 et al., 2022). Large values of  $|\partial u / \partial y|$  at some heights~~s~~, are equivalent in some sense to faster rotation, which restricts the  
534 latitudinal band or waveguide where the diurnal tide can propagate vertically, thus reducing the tidal amplitude above by  
535 removing tidal energy at that altitude (McLandress, 2002b; Siddiqui et al., 2022). The wind shear at 18°N/S ~~are~~is a typical  
536 indicators (Kogure et al., 2021).



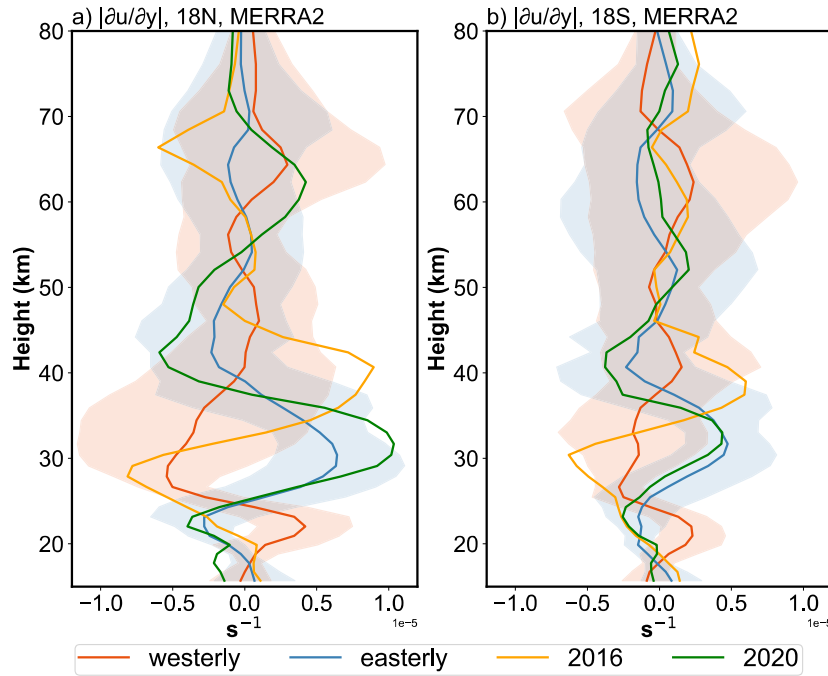


**Figure 10. The  $|\partial u/\partial y|$  profiles after deseasonalized between different QBO phases at (a) 18°N and (b) 18°S. The colourful shaded areas denote one standard deviation of the phases for each height.**

The monthly  $|\partial u/\partial y|$  at 18°N/S is calculated, deseasonalized, and classified following the method described in Section 3.1. The  $|\partial u/\partial y|$  profiles for different QBO phases are shown in Figure 10. During QBOW, a pronounced negative anomaly appears near 30 km, whereas during QBOE a strong positive anomaly is evident at the same altitude. During the 2016 disruption event, the  $|\partial u/\partial y|$  profile at 18°N exhibits a structure broadly similar to that of QBOW. However, from 35 to 45 km it shows ~~strong~~<sup>large</sup> positive values, a feature not observed in other QBO phases. The  $|\partial u/\partial y|$  profile at 18°S displays a similar vertical structure but with smaller amplitudes. Based on this structure, the tide may be amplified near 30 km and subsequently damped near 40 km, which could partly explain why the tidal amplitudes during the 2016 disruption do not reach those observed in QBOW. In contrast, the  $|\partial u/\partial y|$  during the 2020 disruption event closely resembles the QBOE structure, suggesting that the tidal propagation background was similar to QBOE conditions.

#### 4.3 Contribution of Tide-gravity wave interaction during the events

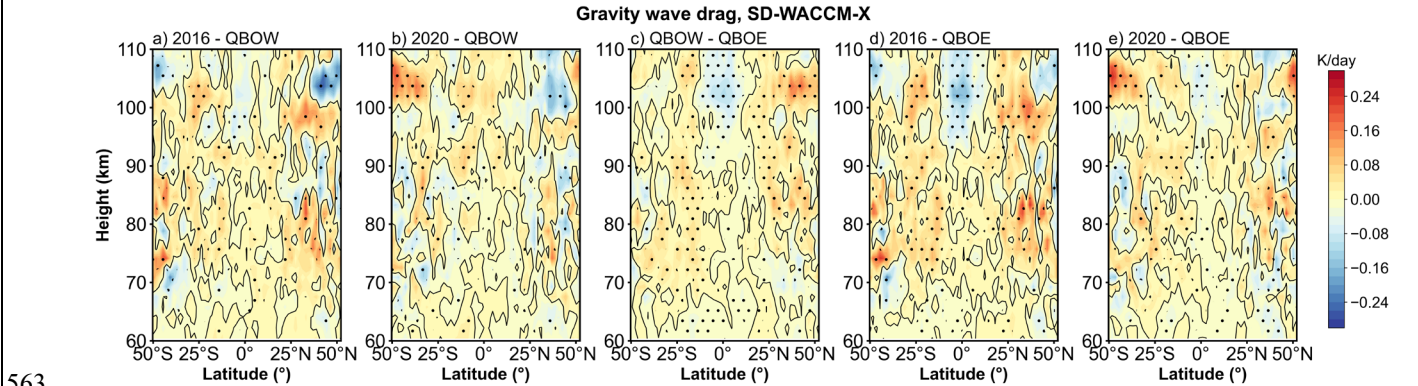
The mesospheric diurnal tides are also affected by the interaction with GWs (Liu and Hagan, 1998; Mayr et al., 1998; ~~McLandress~~<sup>McLandress</sup>, 2002a; Li et al., 2009; Lu et al., 2012; Yang et al., 2018; Stober et al., 2021; Cen et al., 2022). [These interactions can strongly](#) ~~It could greatly~~ modulate tidal amplitude and phase (Liu and Hagan, 1998; Lu et al., 2009; Li et al., 2009; Wang et al., 2024). [In the mesosphere, gravity-wave drag may be linked to the QBO. As discussed in Wang et al. \(2024\), QBO-dependent zonal wind shear and associated zero-wind lines filter the upward-propagating gravity waves that can reach the mesosphere, making the gravity wave drag exhibit QBO-like features. In the tropical region of the mesosphere, due to the](#)

557 [strong interaction between the GWs and the semi-annual oscillation \(SAO\) in zonal wind, the GWs in the mesosphere exhibit](#)  
558 [a weak QBO signature. QBO-related variations in GWs primarily exists in the mid-latitude mesosphere.](#)

559 To quantify the GW forcing on the DW1, the methods of Yang et al. (2018) and Cen et al. (2022) are applied. The equation is:

$$560 \quad GW_{\text{forcing}} = GW_{\text{drag}} \cdot \cos(\omega \cdot (\phi_{\text{GW}} - (\phi_T - 6))) \quad (35)$$

561 Where the  $GW_{\text{drag}}$  is the DW1 amplitude of GW drag,  $\omega$  is the  $24/2\pi$ ,  $\phi_{\text{GW}}$  is the DW1 phase of GW drag while  $\phi_T$  is DW1  
562 amplitude of temperature.



563  
564 **Figure 11. Similar to figure 2 but the difference of gravity wave forcing. (a-e) give the difference result derived from SD-WACCM-**  
565 **X.**

566 After calculating the GW forcing, the classification method [described](#) in Section 3.1 is applied. As shown in Figure [S3D1](#), GW  
567 tends to damp the DW1 amplitude at nearly all latitudes above 105 km. Below ~105 km, the GWs tend to damp the DW1  
568 amplitude at [the equator while enhancing it and strengthen the DW1 amplitude](#) at subtropical [latitudes](#). [Differences exist There](#)  
569 [are differences](#) in the amplitude of gravity wave drag between different QBO phases. Figure 11 shows the differences in GW  
570 forcing between QBO phases, with dots indicating regions exceeding the 95% significance level. During QBOW (Fig. 11c),  
571 the equatorial damping and subtropical enhancement are stronger than during QBOE. During the 2016 QBO disruption event,  
572 the pattern closely resembles the QBOW–QBOE difference but [exhibits with a](#) larger magnitude than QBOW (Fig. 11a). During  
573 the 2020 disruption event, the GW drag is [similarelose](#) to QBOW conditions and is stronger than in QBOE. These results  
574 suggest that GW forcing exerts a significant influence on the modulation of DW1 amplitudes across QBO phases and disruption  
575 events.

## 576 5 Summary

577 In this work, the response of global DW1 amplitudes and phases during QBO disruption events is investigated using SABER  
578 observation, MERRA-2 dataset and SD-WACCM-X simulation results from 2002 to 2023. Additionally, the underlying  
579 mechanisms [associated with these during the events is are](#) explored. The findings are summarized as follows:

580 (1) There ~~is~~ are clear differences in (1, 1) mode vertical phase structure and wavelengths between QBO westerly phases and  
581 easterly phases. The DW1 (1, 1) mode vertical phase structure and wavelengths during these two QBO disruption events ~~is~~ are  
582 similar to ~~that those~~ during QBO westerly phases.

583 (2) ~~In~~ During the 2016 QBO disruption event, DW1 amplitudes are markedly enhanced relative to regular ~~QBO easterly~~  
584 ~~(QBOE) conditions~~ but remain lower than those during QBOW. In the mesosphere and lower thermosphere (MLT), the ~~mean~~  
585 ~~enhancement~~ amplitudes increase by ~~reaches~~ ~1.56 K (~20.5 %) at the equator and ~0.54 K (~14.4 %) at 30° N/S, ~~with peaks~~  
586 ~~of ~2.40 K (~26.5 %) and ~0.87 K (~29.5 %) at the same latitudes~~ yet are smaller than those during QBOW by ~1.22 K (-  
587 10.2 %) at the equator. A pronounced ~~increase~~ difference of the DW1 (1, 1) mode relative to QBOW and QBOE is also evident  
588 in the stratosphere, with amplitudes ~0.21 K (~21%) higher than during QBOE and ~0.15 K (~10.9%) weaker than during  
589 QBOW. ~~(~0.21 K, ~21%).~~

590 By contrast, the 2020 disruption shows only a modest rise in DW1 amplitude relative to the regular QBOE and remain much  
591 weaker than during QBOW. In the MLT, the amplitudes rise by ~~mean enhancement reaches~~ ~0.50 K (~6.0 %) at the equator  
592 and ~0.26 K (~7.7 %) at 30°N/S compared to QBOE, but are smaller than those during QBOW by 2.3 K (~21.1%) and 0.57 K  
593 (~12.0%), respectively, ~~with peak anomalies of ~0.91 K (~11.6 %) at the equator and ~0.31 K (~14.2 %) at 30° N/S, whereas~~  
594 ~~in the stratosphere the DW1 (1, 1) mode increase ~0.18 K (~17 %).~~ In the stratosphere, the amplitudes are about 0.18 K  
595 (~17.0%) larger than during QBOE but ~0.18 K (~12.5%) lower than during QBOW.

596 (3) During the 2016 event, the stronger water vapour radiative heating (~8.3 % relative to QBOE and ~10.9 % relative to  
597 QBOW) and latent heating (22% relative to both QBO phases) enhance the tides at their source region. The enhanced water  
598 vapour radiative heating is jointly modulated by 2016 QBO disruption and 2015/16 El Niño event, whereas the enhanced latent  
599 heating is mainly due to the 2015/16 El Niño event. ~~and latent heating increase by ~8 % and ~22 % relative to QBOE. The~~  
600 ~~zonal wind weak latitudinal shear~~ Weak dissipation (zonal winds) and less tidal energy removal (zonal wind latitudinal shear)  
601 during the tide propagate upward in the lower stratosphere do not ~~tends to enhance~~ suppress DW1 amplitudes, while gravity  
602 waves strengthen DW1 in the subtropics and damp it at the equator. Nevertheless, ~~the~~ a stronger shear near ~40 km likely  
603 prevents DW1 amplitudes from reaching the levels observed during normal QBO westerly phases. ~~Overall, the joint~~  
604 modulation of water-vapor radiative heating, latent heating, weak dissipation, weak energy removal and positive GW drag  
605 contribute to a significant increase in DW1 amplitudes.

606 In contrast, during the 2020 event, only water vapour radiative heating exhibits a clear rise (~5 %). The dissipation and the  
607 tidal energy removal in the stratosphere become larger, ~~whereas the latent heating is close to the QBOE, effectively suppressing~~  
608 DW1 enhancement. ~~The zonal wind latitudinal shear closely resembled those during QBO easterly phases, and the~~ The gravity-  
609 wave effect was weaker than in 2016 but still stronger than in QBOE. Consequently ~~As a result~~, the combined influence of  
610 water-vapor radiative heating and GW drag contribute ~~only~~ to a slight increase in DW1 amplitudes relative to QBOE.

611 This work ~~analyses~~ analyzes ~~the feature~~ how the DW1 varies when the highly unusual wind of QBO occurs. This phenomenon  
612 which is found in responses at different atmospheric layers suggests an atmosphere coupling process. The observations and  
613 model simulations give clear evidence of the connection. The possible link between the lower atmosphere trace gases variation

614 and MLT dynamic features is shown during these unique events. The result gives a window for exploring the mechanism of  
 615 the coupling, providing a basis for future research on the underlying mechanisms.

## 616 **Appendix A: approach for calculating the water vapor radiative heating rate**

617 The heating rate for water vapor mainly follows the method from Groves et al. (1982) and Lieberman et al. (2003).  
 618 As mentioned in equation 1, the heating rate could be categorized into clear sky and cloudy sky. The equation of clear  
 619 sky is given by Lacis and Hansen (1974):

$$620 \quad J_{clr} = q\eta^c S_0 \cos \zeta \left[ MA(y) + \frac{5}{3} RA(y') \right] \quad (A1)$$

621 with  $q$  is water vapor mixing ratio (specific humidity),  $\eta$  is defined as  $p/p_0$ ,  $c$  is defined as  $0.75 - \Gamma R_M/2g$ .  $\Gamma$  is the  
 622 vertical lapse rate, which is  $6.5\text{K km}^{-1}$ .  $R_M$  is the gas constant for air.  $g$  is the acceleration of gravity.  $S_0$  is the solar  
 623 constant, which is  $1353\text{ W m}^{-2}$ .  $\zeta$  is the solar zenith angle, the equation is:

$$624 \quad \cos \zeta = \sin \theta \sin \delta + \cos \theta \cos \delta \cos t' \quad (A2)$$

625 with  $\theta$  is the latitude,  $\delta$  is the solar declination.  $t'$  is given by following equation:

$$626 \quad t' = \lambda + \Omega t \quad (A3)$$

627 with  $\lambda$  is longitude in radian,  $\Omega$  is the angular frequency of Earth's rotation.  $t$  is the universal time.

628  $M$  is given by equation:

$$629 \quad M = \frac{35}{(1224 \cos^2 \zeta + 1)^{\frac{1}{2}}} \quad (A4)$$

630  $A(y)$  is given by equation:

$$631 \quad A(y) = 2.9 \left[ \frac{0.635 + 0.365Y}{(Y^{0.635} + 5.925y)^2 Y^{0.365}} \right] \text{cm}^2 \text{g}^{-1} \quad (A5)$$

632

633 with:

$$634 \quad Y = 1 + 141.5y \quad (A6)$$

635 and

$$636 \quad y = M\bar{w} \quad (A7)$$

637 and

$$638 \quad y' = M\bar{w}_t + \frac{5}{3}(\bar{w}_t - \bar{w}) \quad (A8)$$

639 The  $\bar{w}$  is the effective water vapor amount, is given by equation:

$$\bar{w} = \int_z^\infty q\rho(p/p_0)^{.75}(T_0/T)^{1/2}dz \quad (A9)$$

Where  $\rho$  is the air density.  $\bar{w}_t$  is the total water vapor above the reflecting surface.

The cloudy sky heating rate is given by Groves (1982):

$$J_{cld} = q\eta^c S_0 \cos \zeta Z \quad (A10)$$

with Z is parameter given by:

$$Z = \sum_i \{ak'[\cosh(\xi_0 + \beta - \xi)) - \cosh(\xi_0 + \beta' - \xi)]/\sinh(\xi_0 + \beta)\}_i \quad (A11)$$

with  $\xi$  is given by:

$$\xi = k'\bar{w} \quad (A12)$$

$$k' = \frac{5}{3}\alpha(\sigma + k) \quad (A13)$$

with  $\alpha$ ,  $\beta$  and  $\beta'$ :

$$\alpha = (1 - \omega)^{\frac{1}{2}}(1 + \omega - 2\omega f)^{\frac{1}{2}} \quad (A14)$$

$$\beta = \frac{1}{2}\ln\{[1 + \alpha - \omega f - R\omega(1 - f)] \div [1 - \alpha - \omega f - R\omega(1 - f)]\} \quad (A15)$$

$$\beta' = \beta + \frac{1}{2}\ln\left[\frac{1 - \alpha - \omega f}{1 + \alpha - \omega f}\right] \quad (A16)$$

with single scattering albedo:

$$\omega = \frac{\sigma}{\sigma + k} \quad (A17)$$

where  $\sigma = 40 \text{ cm}^{-1}$ , f is 0.925, k and a are given by table 2 from Somerville et al. (1974).

## Appendix B: approach for calculating the ozone radiative heating rate

The heating rate for ozone mainly uses the equations from Strobel/Zhu model (Strobel, 1978; Zhu, 1999) and processing method from Xu et al. (2010). The Chappius, Hartley and Huggins bands are as follow:

$$\frac{H_{Ch}}{[O_3]} = F_c \sigma_c \exp[-\sigma_c N_3] \quad (B1)$$

$$\frac{H_{Ha}}{[O_3]} = F_{Ha} \sigma_{Ha} \exp[-\sigma_{Ha} N_3] \quad (B2)$$

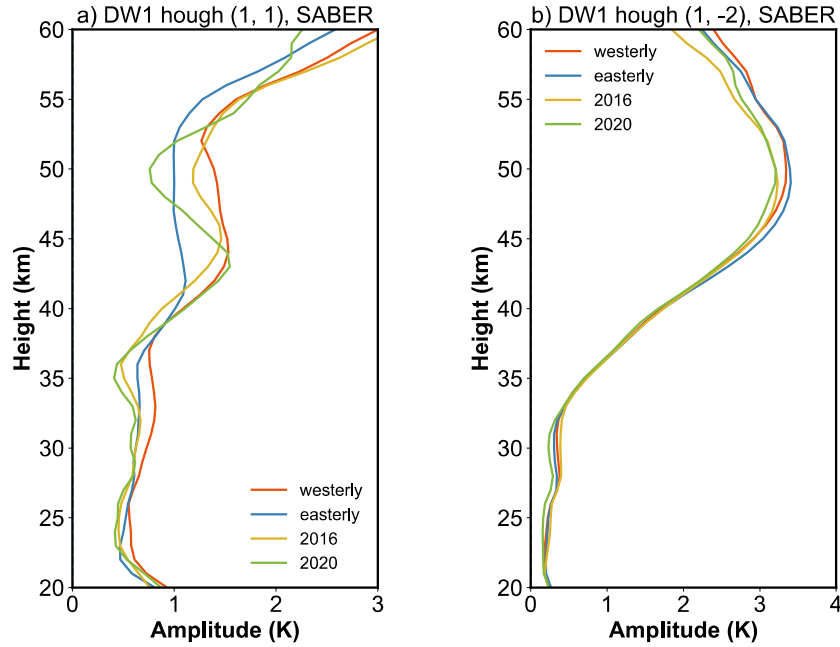
$$\frac{H_{Hu}}{[O_3]} = \frac{1}{MN_3} \{I_1 + (I_2 - I_1) \exp[-\sigma_{Hu} N_3 e^{-M\lambda_{long}}] - I_2 \exp[-\sigma_{Hu} N_3 e^{-M\lambda_{short}}]\} \quad (B3)$$

The  $[O_3]$  is the ozone number density while the  $N_3$  is the column density of  $O_3$  along the solar radiation path. For

663 equation B1, the  $F_c$  is  $370 \text{ J m}^{-2} \text{ s}^{-1}$ , the  $\sigma_c$  is  $2.85 \times 10^{-25}$ . For equation B2, the  $F_{Ha}$  is  $5.13 \text{ J m}^{-2} \text{ s}^{-1}$ , the  $\sigma_{Ha}$  is  $8.7 \times 10^{-22} \text{ m}^{-2}$ . For equation B3, the  $I_1$  is  $0.07 \text{ J m}^{-2} \text{ s}^{-1} \text{ \AA}^{-1}$ , the  $I_2$  is  $0.07 \text{ J m}^{-2} \text{ s}^{-1} \text{ \AA}^{-1}$ ,  $M$  is  $0.01273 \text{ \AA}^{-1}$ ,  $\lambda_{long}$  is  $2805 \text{ \AA}^{-1}$ ,  $\lambda_{short}$  is  $3015 \text{ \AA}^{-1}$ ,  $\sigma_{Hu}$  is  $1.15 \times 10^{-6} \text{ m}^{-2}$ .  
 666 For the heating rate calculation, the ozone density profiles are firstly interpolated to a uniform vertical grid with 1 km spacing  
 667 from 20 km to 105 km. Then the ozone profiles are processing into zonal mean overlapping latitude bins that are 10 degrees  
 668 wide with centres offset by  $5^\circ$  from  $50^\circ\text{S}$ - $50^\circ\text{N}$ . The diurnal variation of the vertical profile of the ozone heating rate in each  
 669 latitude bin is calculated using the SABER ozone density and equation B1-B3, along with the diurnal variation of solar zenith  
 670 angle for the specific latitude and day of year.

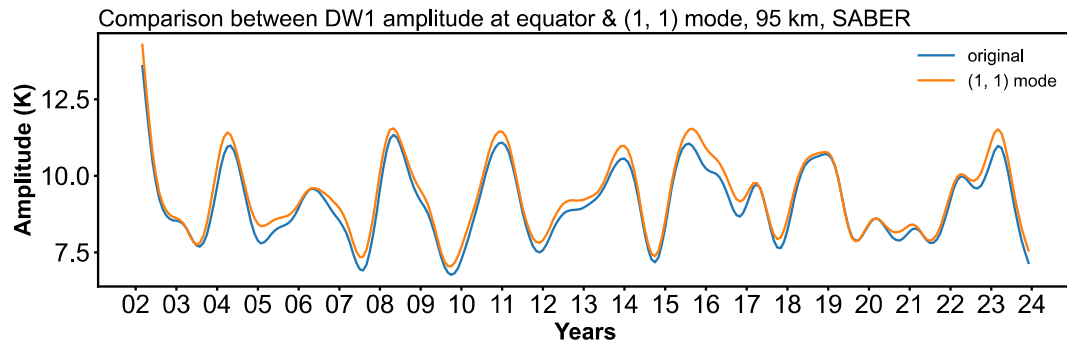
#### 671 Appendix C: The feature of DW1 (1, 1) Hough mode

672



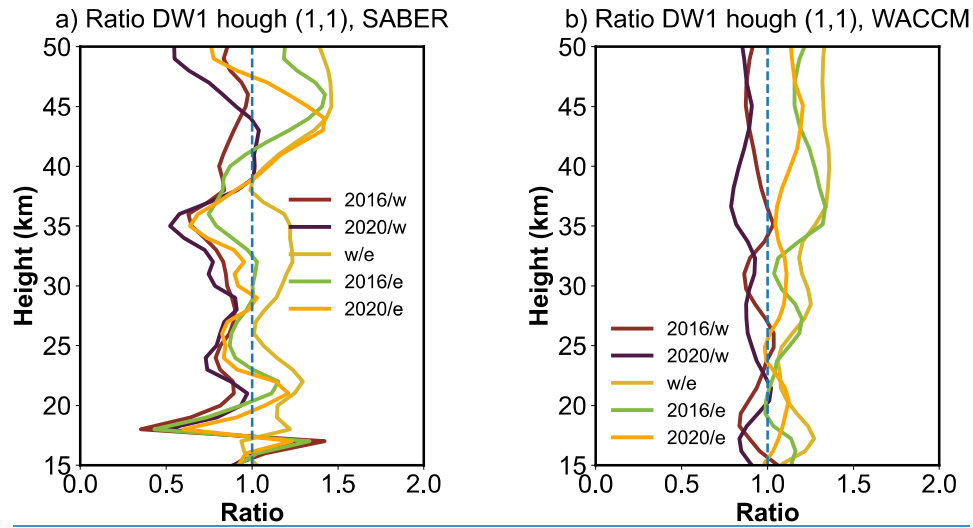
673

674 Figure S1C1. Amplitude profiles of DW1a) (1,1) and b) (1, -2) modes during different QBO phases



675

676 Figure S2C2. The amplitude time series of equatorial DW1 and (1, 1) Hough mode at 95 km.



677

678 Figure C3. the vertical profile of DW1 (1, 1) mode amplitude ratio derived from 2016/westerly (dark red), 2020/westerly (dark  
679 purple), westerly/easterly (yellow), 2016/easterly (green), and 2020/easterly (orange). The dashed blue lines represent the ratio  
680 of 1.

681

682 [Appendix D: Gravity wave drag effect to DW1](#)

683



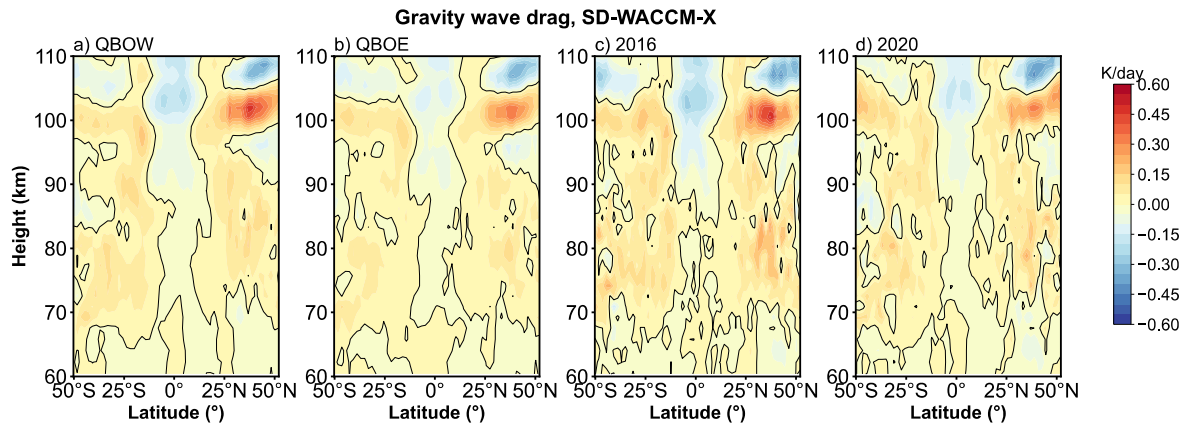


Figure S3D1. The gravity wave forcing on DW1 during difference QBO phases as a function of latitude and altitude

**Data availability.** SABER data is available from the SABER project data server at <https://spdf.gsfc.nasa.gov/pub/data/timed/saber/>. The SD-WACCM-X is retrieved from [https://app.globus.org/file-manager?origin\\_id=d2762023-6ab4-46c9-ab12-b037cd568e42&origin\\_path=%2F](https://app.globus.org/file-manager?origin_id=d2762023-6ab4-46c9-ab12-b037cd568e42&origin_path=%2F). The QBO index is retrieved from [https://acd-ext.gsfc.nasa.gov/Data\\_services/met/qbo/QBO\\_Singapore\\_Uvals\\_GSFC.txt](https://acd-ext.gsfc.nasa.gov/Data_services/met/qbo/QBO_Singapore_Uvals_GSFC.txt). The Generalized Lomb-Scargle Periodogram and best-frequency fit method are provided by PyAstronomy (<https://github.com/sczesla/PyAstronomy>). The MERRA-2 reanalysis data can be retrieved from [https://disc.gsfc.nasa.gov/datasets/M2T3NVASM\\_5.12.4/summary/](https://disc.gsfc.nasa.gov/datasets/M2T3NVASM_5.12.4/summary/) (zonal wind, temperature, cloud fraction, specific humidity), [https://disc.gsfc.nasa.gov/datasets/M2I3NVAER\\_5.12.4/summary](https://disc.gsfc.nasa.gov/datasets/M2I3NVAER_5.12.4/summary) (air density), [https://disc.gsfc.nasa.gov/datasets/M2T1NXRAD\\_5.12.4/summary](https://disc.gsfc.nasa.gov/datasets/M2T1NXRAD_5.12.4/summary) (surface albedo), [https://disc.gsfc.nasa.gov/datasets/M2T3NPTDT\\_5.12.4/summary?keywords=MERRA2%20tdt](https://disc.gsfc.nasa.gov/datasets/M2T3NPTDT_5.12.4/summary?keywords=MERRA2%20tdt) (tendency of air temperature due to moist processes).

**Author contributions.** Conceptualization: SL, GYJ; investigation: SL, GYJ; project administration: BXL, GYJ and YJZ; software: SL; supervision: GYJ, BXL and YJZ; validation: BXL, GYJ and YJZ; visualization: SL; writing – original draft preparation: SL; and writing – review and editing: GYJ, BXL, XL, JYX, YJZ and WY. All authors have read and agreed to the published version of the paper.

**Competing interests.** The authors declare that they have no conflict of interest.

**Disclaimer.** Publisher's note: Copernicus Publications remains neutral with regard to jurisdictional claims made in the text, published maps, institutional affiliations, or any other geographical representation in this paper. While Copernicus Publications makes every effort to include appropriate place names, the final responsibility lies with the authors.

709 **Acknowledgements.** WACCM-X SD output data have been used in this study, and we would like to acknowledge the  
710 WACCM-X development group at NCAR/HAO for making the model output publicly available. This work was jointly  
711 supported by the Strategic Priority Research Program of the Chinese Academy of Sciences (Grant No. XDB0560000),  
712 the Pandeng Program of National Space Science Center CAS, National Key R&D program of China (2023YFB3905100),  
713 the Project of Stable Support for Youth Team in Basic Research Field, CAS (YSBR-018), the National Natural Science  
714 Foundation of China (42174212), the Chinese Meridian Project, and the Specialized Research Fund for State Key  
715 Laboratories.

716

717 **Financial support.** This work was jointly supported by the Strategic Priority Research Program of the Chinese Academy  
718 of Sciences (Grant No. XDB0560000), the Pandeng Program of National Space Science Center CAS, National Key  
719 R&D program of China (2023YFB3905100), the Project of Stable Support for Youth Team in Basic Research Field,  
720 CAS (YSBR-018), the National Natural Science Foundation of China (42174212), the Chinese Meridian Project, and  
721 the Specialized Research Fund for State Key Laboratories.

722

723 **References**

724 Anstey, J. A., Banyard, T. P., Butchart, N., Coy, L., Newman, P. A., Osprey, S., and Wright, C. J.: Prospect of Increased  
725 Disruption to the QBO in a Changing Climate, *Geophys. Res. Lett.*, 48, 10.1029/2021gl093058, 2021.

726 Baldwin, M. P., Gray, L. J., Dunkerton, T. J., Hamilton, K., Haynes, P. H., Randel, W. J., Holton, J. R., Alexander, M. J.,  
727 Hirota, I., Horinouchi, T., Jones, D. B. A., Kinnnersley, J. S., Marquardt, C., Sato, K., and Takahashi, M.: The quasi-biennial  
728 oscillation, *Rev. Geophys.*, 39, 179-229, 10.1029/1999rg000073, 2001.

729 Barton, C. A. and McCormack, J. P.: Origin of the 2016 QBO Disruption and Its Relationship to Extreme El Niño Events,  
730 *Geophys. Res. Lett.*, 44, 10.1002/2017gl075576, 2017.

731 Cen, Y., Yang, C., Li, T., Russell Iii, J. M., and Dou, X.: Suppressed migrating diurnal tides in the mesosphere and lower  
732 thermosphere region during El Niño in northern winter and its possible mechanism, *Atmos. Chem. Phys.*, 22, 7861-7874,  
733 10.5194/acp-22-7861-2022, 2022.

734 Chapman, S. and Lindzen, R.: *Atmospheric tides – thermal and gravitational*, D. Reidel Publishing Company, Dordrecht, the  
735 Netherlands, ISBN 978-94-010-3401-2, 1970.

736 Coy, L., Newman, P. A., Pawson, S., and Lait, L. R.: Dynamics of the Disrupted 2015/16 Quasi-Biennial Oscillation, *J. Clim.*,  
737 30, 5661-5674, 10.1175/jcli-d-16-0663.1, 2017.

738 Davis, R. N., Du, J., Smith, A. K., Ward, W. E., and Mitchell, N. J.: The diurnal and semidiurnal tides over Ascension Island  
 739 ( $^{\circ}$  S,  $14^{\circ}$  W) and their interaction with the stratospheric quasi-biennial oscillation: studies with meteor radar, eCMAM and  
 740 WACCM, *Atmos. Chem. Phys.*, 13, 9543-9564, 10.5194/acp-13-9543-2013, 2013.

741 de Araújo, L. R., Lima, L. M., Jacobi, C., and Batista, P. P.: Quasi-biennial oscillation signatures in the diurnal tidal winds  
 742 over Cachoeira Paulista, Brazil, *J. Atmos. Sol. Terr. Phys.*, 155, 71-78, 10.1016/j.jastp.2017.02.001, 2017.

743 Dhadly, M. S., Emmert, J. T., Drob, D. P., McCormack, J. P., and Niciejewski, R. J.: Short-Term and Interannual Variations  
 744 of Migrating Diurnal and Semidiurnal Tides in the Mesosphere and Lower Thermosphere, *J. Geophys. Res.: Space Phys.*, 123,  
 745 7106-7123, 10.1029/2018ja025748, 2018.

746 Diallo, M., Riese, M., Birner, T., Konopka, P., Müller, R., Hegglin, M. I., Santee, M. L., Baldwin, M., Legras, B., and Ploeger,  
 747 F.: Response of stratospheric water vapor and ozone to the unusual timing of El Niño and the QBO disruption in 2015–2016,  
 748 *Atmos. Chem. Phys.*, 18, 13055-13073, 10.5194/acp-18-13055-2018, 2018.

749 Diallo, M. A., Ploeger, F., Hegglin, M. I., Ern, M., Grooß, J.-U., Khaykin, S., and Riese, M.: Stratospheric water vapour and  
 750 ozone response to the quasi-biennial oscillation disruptions in 2016 and 2020, *Atmos. Chem. Phys.*, 22, 14303-14321,  
 751 10.5194/acp-22-14303-2022, 2022.

752 Ern, M., Ploeger, F., Preusse, P., Gille, J. C., Gray, L. J., Kalisch, S., Mlynyczak, M. G., Russell, J. M., and Riese, M.: Interaction  
 753 of gravity waves with the QBO: A satellite perspective, *J. Geophys. Res.: Atmos.*, 119, 2329-2355, 10.1002/2013jd020731,  
 754 2014.

755 Forbes, J. M. and Vincent, R. A.: Effects of mean winds and dissipation on the diurnal propagating tide: An analytic approach,  
 756 *Planet. Space Sci.*, 37, 197-209, 10.1016/0032-0633(89)90007-x, 1989.

757 Forbes, J. M. and Garrett, H. B.: Seasonal-Latitudinal Structure of the Diurnal Thermospheric Tide, *J. Atmos. Sci.*, 35, 148-  
 758 159, 10.1175/1520-0469(1978)035<0148:Slstod>2.0.Co;2, 1978.

759 Gan, Q., Du, J., Ward, W. E., Beagley, S. R., Fomichev, V. I., and Zhang, S.: Climatology of the diurnal tides from eCMAM30  
 760 (1979 to 2010) and its comparison with SABER, *Earth Planets Space*, 66, 10.1186/1880-5981-66-103, 2014.

761 Garcia, R. R.: On the Structure and Variability of the Migrating Diurnal Temperature Tide Observed by SABER, *J. Atmos.*  
 762 *Sci.*, 80, 687-704, 10.1175/jas-d-22-0167.1, 2023.

763 Garcia, R. R., Marsh, D. R., Kinnison, D. E., Boville, B. A., and Sassi, F.: Simulation of secular trends in the middle atmosphere,  
 764 1950–2003, *J. Geophys. Res.: Atmos.*, 112, 10.1029/2006jd007485, 2007.

765 Gelaro, R., McCarty, W., Suarez, M. J., Todling, R., Molod, A., Takacs, L., Randles, C., Darmenov, A., Bosilovich, M. G.,  
 766 Reichle, R., Wargan, K., Coy, L., Cullather, R., Draper, C., Akella, S., Buchard, V., Conaty, A., da Silva, A., Gu, W., Kim, G.  
 767 K., Koster, R., Lucchesi, R., Merkova, D., Nielsen, J. E., Partyka, G., Pawson, S., Putman, W., Rienecker, M., Schubert, S. D.,  
 768 Sienkiewicz, M., and Zhao, B.: The Modern-Era Retrospective Analysis for Research and Applications, Version 2 (MERRA-  
 769 2), *J Clim*, Volume 30, 5419-5454, 10.1175/JCLI-D-16-0758.1, 2017.

770 Groves, G. V.: Hough components of water vapour heating, *J. Atmos. Terr. Phys.*, 44, 281-290, 10.1016/0021-9169(82)90033-  
 771 2, 1982.

772 Hagan, M. E.: Comparative effects of migrating solar sources on tidal signatures in the middle and upper atmosphere, J.  
773 Geophys. Res.: Atmos., 101, 21213-21222, 10.1029/96jd01374, 1996.

774 Hagan, M. E., Burrage, M. D., Forbes, J. M., Hackney, J., Randel, W. J., and Zhang, X.: QBO effects on the diurnal tide in the  
775 upper atmosphere, Earth Planets Space, 51, 571-578, 10.1186/BF03353216, 1999.

776 Holton, J. R. and Lindzen, R. S.: An Updated Theory for the Quasi-Biennial Cycle of the Tropical Stratosphere, J. Atmos. Sci.,  
777 29, 1076-1080, 10.1175/1520-0469(1972)029<1076:Autftq>2.0.Co;2, 1972.

778 Hu, S. and Fedorov, A. V.: The extreme El Niño of 2015–2016 and the end of global warming hiatus, Geophys. Res. Lett., 44,  
779 3816-3824, 10.1002/2017gl072908, 2017.

780 Jiang, G., Xu, J., Shi, J., Yang, G., Wang, X., and Yan, C.: The first observation of the atmospheric tides in the mesosphere  
781 and lower thermosphere over Hainan, China, Chin. Sci. Bull., 55, 1059-1066, 10.1007/s11434-010-0084-8, 2010.

782 Johnston, B. R., Randel, W. J., and Braun, J. J.: Interannual Variability of Tropospheric Moisture and Temperature and  
783 Relationships to ENSO Using COSMIC-1 GNSS-RO Retrievals, J. Clim., 35, 7109-7125, 10.1175/jcli-d-21-0884.1, 2022.

784 Kang, M.-J. and Chun, H.-Y.: Contributions of equatorial waves and small-scale convective gravity waves to the 2019/20  
785 quasi-biennial oscillation (QBO) disruption, Atmos. Chem. Phys., 21, 9839-9857, 10.5194/acp-21-9839-2021, 2021.

786 Kang, M.-J., Chun, H.-Y., Son, S.-W., Garcia, R. R., An, S.-I., and Park, S.-H.: Role of tropical lower stratosphere winds in  
787 quasi-biennial oscillation disruptions, Sci. Adv., 8, 10.1126/sciadv.abm7229, 2022.

788 Kogure, M. and Liu, H.: DW1 Tidal Enhancements in the Equatorial MLT During 2015 El Niño: The Relative Role of Tidal  
789 Heating and Propagation, J. Geophys. Res.: Space Phys., 126, 10.1029/2021ja029342, 2021.

790 Kogure, M., Liu, H., and Jin, H.: Impact of Tropospheric Ozone Modulation Due To El Niño on Tides in the MLT, Geophys.  
791 Res. Lett., 50, 10.1029/2023gl102790, 2023.

792 Lacis, A. A. and Hansen, J.: A Parameterization for the Absorption of Solar Radiation in the Earth's Atmosphere, J. Atmos.  
793 Sci., 31, 118-133, 10.1175/1520-0469(1974)031<0118:Apftao>2.0.Co;2, 1974.

794 Li, T., She, C. Y., Liu, H. L., Yue, J., Nakamura, T., Krueger, D. A., Wu, Q., Dou, X., and Wang, S.: Observation of local  
795 tidal variability and instability, along with dissipation of diurnal tidal harmonics in the mesopause region over Fort Collins,  
796 Colorado (41°N, 105°W), J. Geophys. Res.: Atmos., 114, 10.1029/2008jd011089, 2009.

797 Lieberman, R. S., Ortland, D. A., and Yarosh, E. S.: Climatology and interannual variability of diurnal water vapor heating, J.  
798 Geophys. Res.: Atmos., 108, 10.1029/2002jd002308, 2003.

799 Lieberman, R. S., Riggan, D. M., Ortland, D. A., Nesbitt, S. W., and Vincent, R. A.: Variability of mesospheric diurnal tides  
800 and tropospheric diurnal heating during 1997–1998, J. Geophys. Res., 112, 10.1029/2007jd008578, 2007.

801 Lindzen, R. S. and Holton, J. R.: A Theory of the Quasi-Biennial Oscillation, J. Atmos. Sci., 25, 1095-1107, 10.1175/1520-  
802 0469(1968)025<1095:Atotqb>2.0.Co;2, 1968.

803 Liu, G., Lieberman, R. S., Harvey, V. L., Pedatella, N. M., Oberheide, J., Hibbins, R. E., Espy, P. J., and Janches, D.: Tidal  
804 Variations in the Mesosphere and Lower Thermosphere Before, During, and After the 2009 Sudden Stratospheric Warming,  
805 J. Geophys. Res.: Space Phys., 126, 10.1029/2020ja028827, 2021.

806 Liu, H. L. and Hagan, M. E.: Local heating/cooling of the mesosphere due to gravity wave and tidal coupling, *Geophys. Res.*  
 807 *Lett.*, 25, 2941-2944, 10.1029/98gl02153, 1998.

808 Liu, H. L., Bardeen, C. G., Foster, B. T., Lauritzen, P., Liu, J., Lu, G., Marsh, D. R., Maute, A., McInerney, J. M., Pedatella,  
 809 N. M., Qian, L., Richmond, A. D., Roble, R. G., Solomon, S. C., Vitt, F. M., and Wang, W.: Development and Validation of  
 810 the Whole Atmosphere Community Climate Model With Thermosphere and Ionosphere Extension (WACCM - X 2.0), *J. Adv.*  
 811 *Model. Earth Syst.*, 10, 381-402, 10.1002/2017ms001232, 2018.

812 Liu, H. L., Foster, B. T., Hagan, M. E., McInerney, J. M., Maute, A., Qian, L., Richmond, A. D., Roble, R. G., Solomon, S.  
 813 C., Garcia, R. R., Kinnison, D., Marsh, D. R., Smith, A. K., Richter, J., Sassi, F., and Oberheide, J.: Thermosphere extension  
 814 of the Whole Atmosphere Community Climate Model, *J. Geophys. Res.: Space Phys.*, 115, 10.1029/2010ja015586, 2010.

815 Liu, M., Xu, J., Liu, H., and Liu, X.: Possible modulation of migrating diurnal tide by latitudinal gradient of zonal wind  
 816 observed by SABER/TIMED, *Science China Earth Sciences*, 59, 408-417, 10.1007/s11430-015-5185-4, 2015.

817 Liu, S., Jiang, G., Luo, B., Xu, J., Lin, R., Zhu, Y., and Liu, W.: Solar Cycle Dependence of Migrating Diurnal Tide in the  
 818 Equatorial Mesosphere and Lower Thermosphere, *Remote Sens.*, 16, 10.3390/rs16183437, 2024a.

819 Liu, Y., Xu, J., Smith, A. K., and Liu, X.: Seasonal and Interannual Variations of Global Tides in the Mesosphere and Lower  
 820 Thermosphere Neutral Winds: I. Diurnal Tides, *J. Geophys. Res.: Space Phys.*, 129, 10.1029/2023ja031887, 2024b.

821 Lu, X., Liu, H. L., Liu, A. Z., Yue, J., McInerney, J. M., and Li, Z.: Momentum budget of the migrating diurnal tide in the  
 822 Whole Atmosphere Community Climate Model at vernal equinox, *J. Geophys. Res.: Atmos.*, 117, n/a-n/a,  
 823 10.1029/2011jd017089, 2012.

824 Lu, X., Liu, A. Z., Swenson, G. R., Li, T., Leblanc, T., and McDermid, I. S.: Gravity wave propagation and dissipation from  
 825 the stratosphere to the lower thermosphere, *J. Geophys. Res.: Atmos.*, 114, 10.1029/2008jd010112, 2009.

826 Marsh, D. R., Mills, M. J., Kinnison, D. E., Lamarque, J.-F., Calvo, N., and Polvani, L. M.: Climate Change from 1850 to  
 827 2005 Simulated in CESM1(WACCM), *J. Clim.*, 26, 7372-7391, 10.1175/jcli-d-12-00558.1, 2013.

828 Mayr, H. G., Mengel, J. G., Talaat, E. R., Porter, H. S., and Chan, K. L.: Mesospheric non-migrating tides generated with  
 829 planetary waves: I. Characteristics, *J. Atmos. Sol. Terr. Phys.*, 67, 959-980, 10.1016/j.jastp.2005.03.002, 2005.

830 Mayr, H. G., Mengel, J. G., Chan, K. L., and Porter, H. S.: Seasonal variations of the diurnal tide induced by gravity wave  
 831 filtering, *Geophys. Res. Lett.*, 25, 943-946, 10.1029/98gl00637, 1998.

832 McLandress, C.: The Seasonal Variation of the Propagating Diurnal Tide in the Mesosphere and Lower Thermosphere. Part I:  
 833 The Role of Gravity Waves and Planetary Waves, *J. Atmos. Sci.*, 59, 893-906, 10.1175/1520-  
 834 0469(2002)059<0893:Tsvotp>2.0.Co;2, 2002a.

835 McLandress, C.: The Seasonal Variation of the Propagating Diurnal Tide in the Mesosphere and Lower Thermosphere. Part  
 836 II: The Role of Tidal Heating and Zonal Mean Winds, *J. Atmos. Sci.*, 59, 907-922, 10.1175/1520-  
 837 0469(2002)059<0907:Tsvotp>2.0.Co;2, 2002b.

838 Mertens, C. J.: SABER observations of mesospheric temperatures and comparisons with falling sphere measurements taken  
 839 during the 2002 summer MaCWAVE campaign, *Geophys. Res. Lett.*, 31, 10.1029/2003gl018605, 2004.

840 Mertens, C. J., Mlynczak, M. G., López-Puertas, M., Wintersteiner, P. P., Picard, R. H., Winick, J. R., Gordley, L. L., and  
 841 Russell, J. M.: Retrieval of mesospheric and lower thermospheric kinetic temperature from measurements of CO<sub>2</sub> 15  $\mu$ m Earth  
 842 Limb Emission under non-LTE conditions, *Geophys. Res. Lett.*, 28, 1391-1394, 10.1029/2000gl012189, 2001.  
 843 Mlynczak, M. G., Hunt, L. A., Garcia, R. R., Harvey, V. L., Marshall, B. T., Yue, J., Mertens, C. J., and Russell, J. M., 3rd:  
 844 Cooling and Contraction of the Mesosphere and Lower Thermosphere From 2002 to 2021, *J Geophys Res Atmos*, 127,  
 845 e2022JD036767, 10.1029/2022JD036767, 2022.  
 846 Mlynczak, M. G., Marshall, B. T., Garcia, R. R., Hunt, L., Yue, J., Harvey, V. L., Lopez-Puertas, M., Mertens, C., and Russell,  
 847 J.: Algorithm Stability and the Long-Term Geospace Data Record From TIMED/SABER, *Geophys. Res. Lett.*, 50,  
 848 10.1029/2022gl102398, 2023.  
 849 Mukhtarov, P., Pancheva, D., and Andonov, B.: Global structure and seasonal and interannual variability of the migrating  
 850 diurnal tide seen in the SABER/TIMED temperatures between 20 and 120 km, *J. Geophys. Res.: Space Phys.*, 114, n/a-n/a,  
 851 10.1029/2008ja013759, 2009.  
 852 Newman, P. A., Coy, L., Pawson, S., and Lait, L. R.: The anomalous change in the QBO in 2015-2016, *Geophys. Res. Lett.*,  
 853 43, 8791-8797, 10.1002/2016gl070373, 2016.  
 854 Neale, R., Richter, J. H., Conley, A. J., Park, S., Lauritzen, P. H., Gettelman, A., Williamson, D., Rasch, P. J., Vavrus, S. J.,  
 855 Taylor, M. A., Collins, W., Zhang, M., & LIN, S. (2010). Description of the NCAR Community Atmosphere Model (CAM  
 856 4.0), 10.5065/GSEB-6470, 2010  
 857 Oberheide, J., Forbes, J. M., Häusler, K., Wu, Q., and Bruinsma, S. L.: Tropospheric tides from 80 to 400 km: Propagation,  
 858 interannual variability, and solar cycle effects, *J. Geophys. Res.: Atmos.*, 114, 10.1029/2009jd012388, 2009.  
 859 Ortland, D. A.: Daily estimates of the migrating tide and zonal mean temperature in the mesosphere and lower thermosphere  
 860 derived from SABER data, *J. Geophys. Res.: Atmos.*, 122, 3754-3785, 10.1002/2016jd025573, 2017.  
 861 Osprey, S. M., Butchart, N., Knight, J. R., Scaife, A. A., Hamilton, K., Anstey, J. A., Schenzinger, V., and Zhang, C.: An  
 862 unexpected disruption of the atmospheric quasi-biennial oscillation, *Science*, 353, 1424-1427, 10.1126/science.aah4156, 2016.  
 863 Pedatella, N.: Ionospheric Variability during the 2020–2021 SSW: COSMIC-2 Observations and WACCM-X Simulations,  
 864 *Atmosphere*, 13, 10.3390/atmos13030368, 2022.  
 865 Pramitha, M., Kishore Kumar, K., Venkat Ratnam, M., Praveen, M., and Rao, S. V. B.: Disrupted Stratospheric QBO  
 866 Signatures in the Diurnal Tides Over the Low-Latitude MLT Region, *Geophys. Res. Lett.*, 48, 10.1029/2021gl093022, 2021a.  
 867 Pramitha, M., Kumar, K. K., Ratnam, M. V., Praveen, M., and Bhaskara Rao, S. V.: Stratospheric Quasi Biennial Oscillation  
 868 Modulations of Migrating Diurnal Tide in the Mesosphere and Lower Thermosphere Over the Low and Equatorial Latitudes,  
 869 *J. Geophys. Res.: Space Phys.*, 126, 10.1029/2020ja028970, 2021b.  
 870 Qian, L., Emery, B. A., Foster, B., Lu, G., Maute, A., Richmond, A. D., et al.: The NCAR TIE-GCM: A community model of  
 871 the coupled thermosphere/ionosphere system. In J. Huba, R. Schunk, & G. Khazanov (Eds.), *Modeling the ionosphere-*  
 872 *thermosphere system*, John Wiley, 73–83, 10.1002/9781118704417.ch7, 2014

873 Riggins, D. M. and Lieberman, R. S.: Variability of the diurnal tide in the equatorial MLT, *J. Atmos. Sol. Terr. Phys.*, 102, 198-  
874 206, 10.1016/j.jastp.2013.05.011, 2013.

875 Sakazaki, T., Fujiwara, M., and Shiotani, M.: Representation of solar tides in the stratosphere and lower mesosphere in state-  
876 of-the-art reanalyses and in satellite observations, *Atmos. Chem. Phys.*, 18, 1437-1456, 10.5194/acp-18-1437-2018, 2018.

877 Sakazaki, T., Fujiwara, M., and Zhang, X.: Interpretation of the vertical structure and seasonal variation of the diurnal  
878 migrating tide from the troposphere to the lower mesosphere, *J. Atmos. Sol. Terr. Phys.*, 105-106, 66-80,  
879 10.1016/j.jastp.2013.07.010, 2013.

880 Santoso, A., McPhaden, M. J., and Cai, W.: The Defining Characteristics of ENSO Extremes and the Strong 2015/2016 El  
881 Niño, *Rev. Geophys.*, 55, 1079-1129, 10.1002/2017rg000560, 2017.

882 Schoeberl, M. R., Douglass, A. R., Newman, P. A., Lait, L. R., Lary, D., Waters, J., Livesey, N., Froidevaux, L., Lambert, A.,  
883 Read, W., Filipiak, M. J., and Pumphrey, H. C.: QBO and annual cycle variations in tropical lower stratosphere trace gases  
884 from HALOE and Aura MLS observations, *J. Geophys. Res.: Atmos.*, 113, 10.1029/2007jd008678, 2008.

885 Siddiqui, T. A., Chau, J. L., Stolle, C., and Yamazaki, Y.: Migrating solar diurnal tidal variability during Northern and Southern  
886 Hemisphere Sudden Stratospheric Warmings, *Earth Planets Space*, 74, 10.1186/s40623-022-01661-y, 2022.

887 Singh, D. and Gurubaran, S.: Variability of diurnal tide in the MLT region over Tirunelveli (8.7°N), India: Consistency  
888 between ground- and space-based observations, *J. Geophys. Res.: Atmos.*, 122, 2696-2713, 10.1002/2016jd025910, 2017.

889 Smith, A. K.: Global Dynamics of the MLT, *Surv. Geophys.*, 33, 1177-1230, 10.1007/s10712-012-9196-9, 2012.

890 Smith, A. K., Pedatella, N. M., Marsh, D. R., and Matsuo, T.: On the Dynamical Control of the Mesosphere–Lower  
891 Thermosphere by the Lower and Middle Atmosphere, *J. Atmos. Sci.*, 74, 933-947, 10.1175/jas-d-16-0226.1, 2017.

892 Smith, A. K., Harvey, V. L., Mlynyczak, M. G., Funke, B., García-Comas, M., Hervig, M., Kaufmann, M., Kyrölä, E., López-  
893 Puertas, M., McDade, I., Randall, C. E., Russell, J. M., Sheese, P. E., Shiotani, M., Skinner, W. R., Suzuki, M., and Walker,  
894 K. A.: Satellite observations of ozone in the upper mesosphere, *J. Geophys. Res.: Atmos.*, 118, 5803-5821, 10.1002/jgrd.50445,  
895 2013.

896 Somerville, R. C. J., Stone, P. H., Halem, M., Hansen, J. E., Hogan, J. S., Druyan, L. M., Russell, G., Lacis, A. A., Quirk, W.  
897 J., and Tenenbaum, J.: The GISS Model of the Global Atmosphere, *J. Atmos. Sci.*, 31, 84-117, 10.1175/1520-  
898 0469(1974)031<0084:Tgmotg>2.0.Co;2, 1974.

899 Sun, R., Gu, S., Dou, X., and Li, N.: Tidal Structures in the Mesosphere and Lower Thermosphere and Their Solar Cycle  
900 Variations, *Atmosphere*, 13, 10.3390/atmos13122036, 2022.

901 Stober, G., Kuchar, A., Pokhotelov, D., Liu, H., Liu, H.-L., Schmidt, H., Jacobi, C., Baumgarten, K., Brown, P., Janches, D.,  
902 Murphy, D., Kozlovsky, A., Lester, M., Belova, E., Kero, J., and Mitchell, N.: Interhemispheric differences of mesosphere–  
903 lower thermosphere winds and tides investigated from three whole-atmosphere models and meteor radar observations, *Atmos.*  
904 *Chem. Phys.*, 21, 13855-13902, 10.5194/acp-21-13855-2021, 2021.

905 Strobel, D. F.: Parameterization of the atmospheric heating rate from 15 to 120 km due to O<sub>2</sub> and O<sub>3</sub> absorption of solar  
906 radiation, *J. Geophys. Res.: Oceans*, 83, 6225-6230, 10.1029/JC083iC12p06225, 1978.



907 Tweedy, O. V., Kramarova, N. A., Strahan, S. E., Newman, P. A., Coy, L., Randel, W. J., Park, M., Waugh, D. W., and Frith,  
 908 S. M.: Response of trace gases to the disrupted 2015–2016 quasi-biennial oscillation, *Atmos. Chem. Phys.*, 17, 6813-6823,  
 909 10.5194/acp-17-6813-2017, 2017.

910 Vincent, R. A., Kovalam, S., Fritts, D. C., and Isler, J. R.: Long-term MF radar observations of solar tides in the low-latitude  
 911 mesosphere: Interannual variability and comparisons with the GSWM, *J. Geophys. Res.: Atmos.*, 103, 8667-8683,  
 912 10.1029/98jd00482, 1998.

913 Wang, J., Li, N., Yi, W., Xue, X., Reid, I. M., Wu, J., Ye, H., Li, J., Ding, Z., Chen, J., Li, G., Tian, Y., Chang, B., Wu, J., and  
 914 Zhao, L.: The impact of quasi-biennial oscillation (QBO) disruptions on diurnal tides over the low- and mid-latitude  
 915 mesosphere and lower thermosphere (MLT) region observed by a meteor radar chain, *Atmos. Chem. Phys.*, 24, 13299-13315,  
 916 10.5194/acp-24-13299-2024, 2024.

917 Wang, Y., Rao, J., Lu, Y., Ju, Z., Yang, J., and Luo, J.: A revisit and comparison of the quasi-biennial oscillation (QBO)  
 918 disruption events in 2015/16 and 2019/20, *Atmos. Res.*, 294, 10.1016/j.atmosres.2023.106970, 2023.

919 Wu, D. L., McLandress, C., Read, W. G., Waters, J. W., and Froidevaux, L.: Equatorial diurnal variations observed in UARS  
 920 Microwave Limb Sounder temperature during 1991–1994 and simulated by the Canadian Middle Atmosphere Model, *J.*  
 921 *Geophys. Res.: Atmos.*, 103, 8909-8917, 10.1029/98jd00530, 1998.

922 Wu, Q., Ortland, D. A., Killeen, T. L., Roble, R. G., Hagan, M. E., Liu, H. L., Solomon, S. C., Xu, J., Skinner, W. R., and  
 923 Niciejewski, R. J.: Global distribution and interannual variations of mesospheric and lower thermospheric neutral wind diurnal  
 924 tide: 1. Migrating tide, *J. Geophys. Res.: Space Phys.*, 113, n/a-n/a, 10.1029/2007ja012542, 2008.

925 Xu, J., Smith, A. K., Jiang, G., and Yuan, W.: Seasonal variation of the Hough modes of the diurnal component of ozone  
 926 heating evaluated from Aura Microwave Limb Sounder observations, *J. Geophys. Res.: Atmos.*, 115, 10.1029/2009jd013179,  
 927 2010.

928 Xu, J., Smith, A. K., Yuan, W., Liu, H. L., Wu, Q., Mlynczak, M. G., and Russell, J. M.: Global structure and long-term  
 929 variations of zonal mean temperature observed by TIMED/SABER, *J. Geophys. Res.*, 112, 10.1029/2007jd008546, 2007.

930 Xu, J., Smith, A. K., Liu, H. L., Yuan, W., Wu, Q., Jiang, G., Mlynczak, M. G., Russell, J. M., and Franke, S. J.: Seasonal and  
 931 quasi-biennial variations in the migrating diurnal tide observed by Thermosphere, Ionosphere, Mesosphere, Energetics and  
 932 Dynamics (TIMED), *J. Geophys. Res.*, 114, 10.1029/2008jd011298, 2009.

933 Yang, C., Smith, A. K., Li, T., and Dou, X.: The Effect of the Madden - Julian Oscillation on the Mesospheric Migrating  
 934 Diurnal Tide: A Study Using SD - WACCM, *Geophys. Res. Lett.*, 45, 5105-5114, 10.1029/2018gl077956, 2018.

935 Zhu, X.: An Accurate and Efficient Radiation Algorithm for Middle Atmosphere Models, *J. Atmos. Sci.*, 51, 3593-3614,  
 936 10.1175/1520-0469(1994)051<3593:Aaaera>2.0.Co;2, 1994.